Flight Test Optimization of Fixed-Wing and Rotary-Wing Unmanned Aerial Vehicles for Planetary Boundary Layer Research

A Thesis Presented for the

Master of Science

Degree

The University of Tennessee, Knoxville

Brittany Lane Porcelli

May 2020

ACKNOWLEDGEMENTS

I would like to thank the Dr. Steve Brooks for his continued support and guidance throughout the duration of this project and my time in graduate school. I would also like to thank Temple Lee, Ed Dumas, Michael Buban, and Bruce Baker at NOAA Air Resources Lab, Atmospheric Turbulence and Diffusion Division in Oak Ridge, Tennessee for allowing me to opportunity to learn from them, participate in the short term field deployments, and use their equipment and facilities during the summer. I would like to acknowledge my committee members, Steve Brooks, Peter Solies, Temple Lee and Trevor Moeller, for their support on my research. Finally, I would like to thank my husband, Drew Porcelli, for his love and inspiring advice throughout my time as a master's candidate.

ABSTRACT

Current methods for atmospheric measurements, such as radiosondes, have limitations in providing adequate data collection in Earth's planetary boundary layer. Technology has presented scientists with the opportunity to replace traditional weather and climate data gathering technology with the use of unmanned aerial vehicles (UAV). UAV technology allows researchers to obtain customized resolution data, reduce the amount of debris contributed by radiosondes, and have a reusable system in place to satisfy the daily need for atmospheric boundary layer information that directly contributes to weather forecasting and agricultural needs. In this thesis, we have flight tested and evaluated two UAV types, fixed-wing and the rotary-wing, as reusable substitutes for the single-use balloon-borne radiosondes. The rotary-wing UAV, Meteomatics Meteodrone SSE, obtained vertical profile measurements of temperature and humidity. The fixed-wing UAV, Blackswift Technologies S2, gathered the identical atmospheric properties in a vertical up-and-down spiral flight. Utilizing constant climb and descent rates, researchers pose the risk of over or under sampling essential layers within the boundary layer. In order to ensure adequate sampling data is captured throughout the boundary layer diurnal cycle, example flight optimization profiles are presented for the typical early morning, midday and nocturnal stages of the atmospheric boundary layer. Optimization includes creating a series of horizontal and vertical steps to allow enough time for sensors to optimally capture data among the transitioning layers. This will generate a precise stair step flight pattern that can be readily programmed for unmanned aircraft. Flight profile optimization can essentially match the use of a tethered balloon system for high resolution in the lower boundary layer but providing the freedom of untethered flight with unlimited altitude capabilities.

TABLE OF CONTENTS

LIST OF TABLES

LIST OF FIGURES

LIST OF SYMBOLS

α	Angle of Attack [°]
γ	Climb Angle [°]
η_p	Propulsive Efficiency
ρ	Atmospheric Density [kg/m^3]
A	Wing Span Ratio
b	Wing Span [m]
C_D	Drag Coefficient
C_{Di}	Lift Induced Drag Coefficient
C_{Do}	Zero Lift Drag Coefficient
C_L	Lift Coefficient
$C_{L\alpha}$	Maximum Lift Coefficient
C_{Ps}	Specific Fuel Consumption [g/kN·s]
D	Drag [N]
E	Endurance [hrs]
e	Oswald Span Efficiency
K	Induced Drag Factor
L	Lift [N]
(L/D)	Lift to Drag Ratio
P_e	Engine Power [kW]
P_{av}	Power Available [kW]
P_{req}	Power Required [kW]
R	Range [km]
ROC	Rate of Climb [m/s]
S	Wing Area [m^2]
T	Thrust [N]
T(V)	Thrust Power [N·m/s]
V	Speed [m/s]
W	Weight [kg]

CHAPTER 1

HISTORY OF OBSERVATION PLATFORMS FOR ATMOPSHERIC BOUNDARY LAYER

1.1 Introduction to the Atmospheric Boundary Layer

The atmospheric boundary layer can be generally described as the turbulent mixing layer that sits 1-2 km above Earth's surface. It has also been known to be described as the lowest section of the troposphere that is quickly influenced, with a time scale of half an hour, by the physical properties of the Earth's surface (Wallace, 2006). Static stability and turbulence combine to squeeze a powerful stable layer between the layer below and the rest of the free atmosphere above. This stable layer referred to as the capping inversion, traps turbulence, moisture, and pollutants below it, and blocks most of the surface friction from being transferred to the troposphere. Thus, creating a distinct atmospheric layer where scientists can study its unique turbulent flow and interaction with the planetary surface (Wallace, 2006).

The atmospheric boundary layer (ABL), from its changing nature and strong gradients, has been difficult to sample in high resolution, yet adequate data collections of this zone are essential to weather prediction and agricultural needs (Lee T. B., 2019). Current methods for atmospheric measurements, such as tether balloons, kytoons and radiosondes, have limitations in providing accurate data collection in Earth's ABL. In more recent years, atmospheric researchers have turned to introducing the use of unmanned aerial vehicles (UAVs) to sample properties within the ABL. This emerging aviation technology can allow researchers to make many advancements in boundary layer measurements and research. Reusable autonomous UAVs can save money, deliver higher resolution data, and eliminate the debris of lost non-reusable balloons/payloads.

However, a major factor to understanding the boundary layer behavior is to comprehend its changing properties during different solar heating and radiative cooling stages within the diurnal cycle. While attempting to sample the ABL, it is best that UAV mission planners consider the rapidly changing layers in order to correctly identify ABL characteristics. In a conventional daytime evolution of the ABL, solar heating causes the thermal plumes within the layer to rise. These plumes climb and expand adiabatically until a thermodynamic equilibrium is achieved near the top of the ABL. Moisture, heat and aerosols are transferred by the plumes and eventually may form convective clouds. Sublayers within the ABL are formed and are individually characterized by the turbulence gradients, mean winds, and radiative flux properties (Wallace, 2006). These sublayers are expanded on in detail in Chapter 3.

The behavior of the atmospheric boundary layer changes from sunset to sunrise causing scientists to denote it as the nocturnal boundary layer (Wallace, 2006). It is characterized by a stable layer which forms when the solar heating halts and the radiative cooling stabilize the lowest part of the ABL. Above that, the remaining properties of the daytime convective boundary layer form the residual layer. The nocturnal boundary layer may also be convective when cold air transports over a warm surface (Wallace, 2006). Figure 1 below shows a diagram of Earth's atmospheric boundary layer.

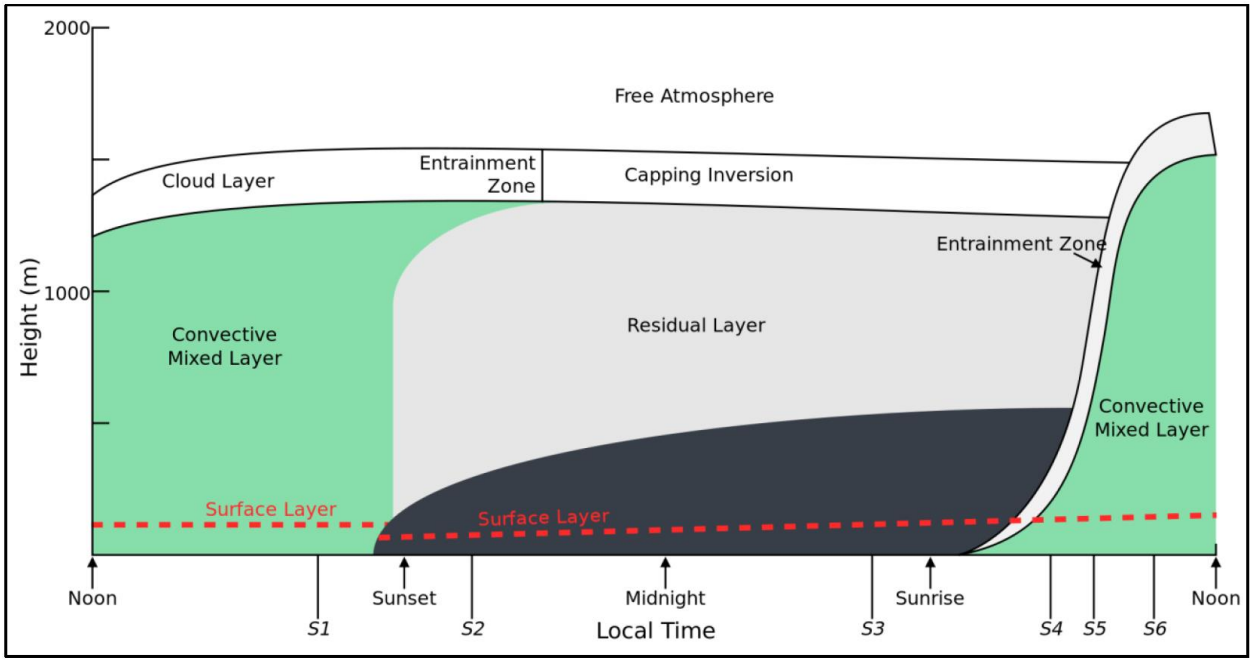

Figure 1: Earth's Boundary Layer transitioning to Nocturnal Boundary Layer (Wallace, 2006)

Turbulent flow is one of the main characteristics of the atmospheric boundary layer. The term turbulence can simply be described as a chaotic or unsteady movement of air, water, or of some other fluid (Wallace, 2006). Wind shear of the mean wind within the boundary layer, caused by drag near the ground, generates vertical velocity gradients that are the main driver of turbulent flow. Inside and outside the ABL, turbulence can be increased by buoyancy, vertical wind shear, or orographic flow. Orographic flow is wind flow caused, affected, or influenced by surface objects like mountains. The terrain shape controls the 3-D motion of the flow, causing speeds to increase and decrease over certain topographic areas (Wallace, 2006).

Turbulence is inspiringly complex and consists of a superposition of swirls on the mean wind that interact nonlinearly to create chaotic motions. The swirls, referred to as eddies, are evanescent and cascade through a succession of progressively smaller eddies until they dissipate. However, a smooth atmospheric flow, laminar flow, can also be present in the boundary layer at

the different locations and times. Eddies are the essential characteristics of turbulence (Wallace, 2006). The original air parcel motion and length of travel directly define the integral eddy length. Integral length eddies within the ABL typically go through 0.5 to 1.0 rotations and can be up to 2 km in size before cascading into smaller eddies and eventually dissipating into heat. Air parcel motion itself can occur from multiple atmospheric factors including orographic flow, buoyancy rising and sinking, transfer of horizontal momentum, cold front movements, and radiative transfer. The transfer of horizontal momentum from a high area to a lower area from parcel motion is the main action of turbulence and can help calculate eddy lengths within the ABL (Wallace, 2006). During the cascading succession, the internal energy of the largest eddies is transferred to the smaller eddies before dissipation. This internal energy is can be quantified to indicate how much Turbulence Kinetic energy (TKE) is present. TKE is continually dissipated into the internal energy by molecular viscosity at the smallest eddy size (Wallace, 2006). Figure 2 below shows the TKE spectrum compared to eddy size.

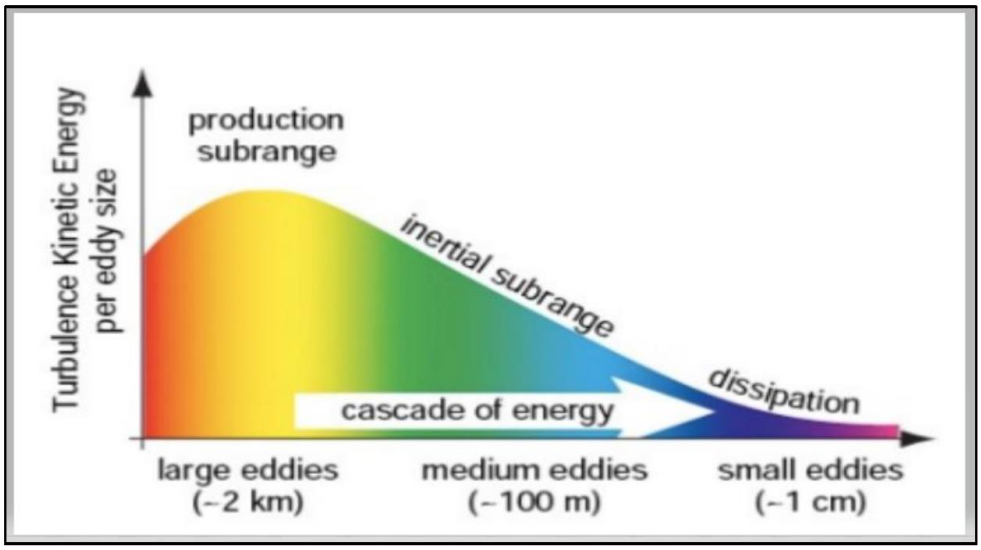

Figure 2: Turbulence Kinetic Energy Spectrum (Wallace, 2006)

Due to the turbulent nature of the boundary layer dynamics, if researchers were to simply pilot the UAV at a constant rate of climb and descent, there is a high probability that the upper layers within the ABL would be oversampled and the surface layer itself would be under sampled. Thus, optimizing UAV flight profiles while piloting within the ABL would give researchers the highest quality of data and the shortest flight times for UAV operations. In order to determine accurate optimizations within the ABL, we need to first examine how current observation methods fall short in providing accurate ABL sampling.

1.2 History and Usage of Radiosondes

A radiosonde is a balloon-borne device that measures the vertical profile of atmospheric variables and transmits data to a ground-based station (Pommereau, 2003). Typically, the profiles of temperature, humidity and pressure with height captured by radiosondes are received by the ground station with twice a day launches, and provide valuable input for numerical weather forecasting models (Pommereau, 2003). Key advantages of the radiosonde are its simplicity and ability to sample from the surface up to several kilometers (Flores, 2013). In some cases, the ascent of the radiosonde provides indirect wind speed and direction measurements throughout the troposphere. The first radiosonde was first deployed by a Russian meteorologist, Pavel A. Molchanov, in 1930. However, it wasn't until 1936 when the U.S. Weather Bureau starting using this technology on a routine basis. Thus, the radiosonde is often referred to as the fundamental instrument of meteorological research (Flores, 2013). In 2012, there were 92 operational radiosonde stations in the United States, which made a daily average of over 200 soundings every day in support of weather forecast activities, and over 800 radiosonde stations worldwide (Pommereau, 2003).

The radiosonde is flown by a latex or neoprene balloon as part of a flight train. Radiosonde systems typically use a balloon that weighs from 300 to 1200 grams, and are filled with helium or hydrogen gas to ensure an ascent rate of 5 m/s (Pommereau, 2003). The radiosonde flight train includes the five following parts:

1. The balloon
2. The parachute to return the radiosonde back safely
3. 20 to 60m of nylon separation line which isolates the sensors from the balloon
4. The de-reeler or unwinder to release the nylon line shortly after launch
5. The radiosonde equipped with sensors to capture samples

The radiosonde itself includes a suite of meteorological sensors, signal-processing electronics, and a radio transmitter to send the measurements to the ground stations (Pommereau, 2003). Figure 3 below shows the full radiosonde flight train with its five numbered components.

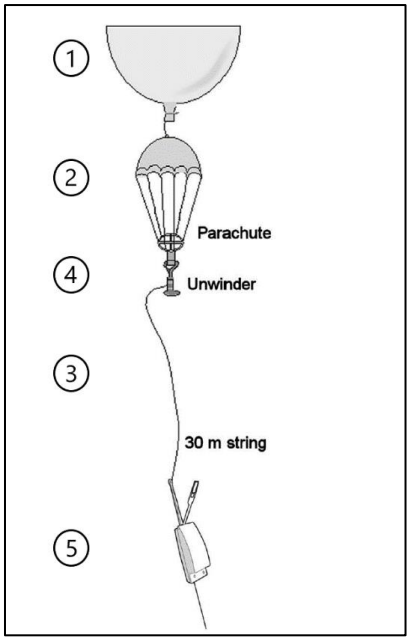

Figure 3: Radiosonde with Numbered Components (Pommereau, 2003)

The weather sensing instruments located inside the radiosonde include a thermistor, hygristor, aneroid barometer, and a baroswitch. The resistance thermistor serves as a temperature sensor while the hygristor serves as a humidity sensor. Both devices use electrical resistance as a means to measure changes within the atmosphere. The aneroid barometer measures the pressure by using a small metal canister that expands in response to the reduction in atmospheric pressure. Lastly, the barometer is a switching mechanism, usually used on older radiosonde models, to switch between the two sensor and reference elements. It also has a contact arm that passes over a communicator bar, which includes a conducting strip and insulator strip that both transmit humidity and temperature information (Pommereau, 2003).

Most radiosondes also include a miniature radio transmitter that generates an FM radio frequency to send the sampling information to the ground station below. Additionally, a small battery is also included within the radiosonde to serve as a power supply for the sensors and radio transmitter. Current radiosondes have evolved into a relatively standard set of instruments which are vital for sampling the troposphere (Flores, 2013). Several technological advancements of the radiosonde have led to consist use in meteorological sampling over the past 84 years. However, they only provide a brief snapshot of the ABL and are generally released only twice daily from distributed locations. For atmospheric boundary layer research, radiosonde can provide a far more limited amount of sampling information compared to UAVs.

1.3 Limitations of Radiosondes

As groundbreaking as the radiosonde technology was for the NOAA National Weather Service (NWS), today boundary layer researchers require more sophisticated approaches to measuring high resolution meteorological data within the ABL. As mentioned previously, the radiosonde's rate of climb is controlled by the amount of hydrogen or helium gas filled within

the flight balloon. The average radiosonde has an ascent rate of 5 m/s that cannot be controlled or altered during flight. This constant vertical sampling flight path often neglects to achieve an optimal or adequate sample resolution of each layer within the ABL. In order to accurately sample the ABL, it is also imperative that researchers are able to control the flight path of the meteorological vehicle to allow time for each sensor to gather samples in each evolving turbulent layer. This flight path optimization is further explained in Chapter 5 of this thesis.

Additionally, radiosondes produce debris when the balloon/payloads are typically not recovered. In the United States, it is estimated that only 10–15% of radiosondes are recovered and reused after extensive refurbishment (Pommereau, 2003). Although the balloon itself is latex and will gradually biodegrade over time, the real issue lies in the leftover batteries and plastics used in the radiosonde and lines. The batteries can pose an environmental toxicity risk and even a fire hazard if it is a lithium ion type. Also, the balloons and payloads could fall into the ocean, contributing to the already high plastic pollution contents. The majority of countries around the world do not have a retrieval process set in place for used radiosonde debris, which is troubling from an environmental standpoint. The use of UAVs to measure the daily activities within the troposphere can greatly cut the use of radiosondes and, in turn, reduce the pollution left by balloons and payloads. Reusing UAVs for atmospheric research would also help save costs of not having to repurchase radiosondes from companies, such as Vaisala, to replace each lost device. Non-renewable helium would also be conversed. Figure 4 below shows a recovered radiosonde payload.

Figure 4: Recovered Radiosonde Payload

1.4 History and Usage of Tether Balloons and Kytoons

Although radiosondes are used more frequently for troposphere sampling, there are other observational platforms used in atmospheric research. Tethered balloons are unique observation platforms for studying the atmosphere and have been used for research purposes for a long time. In contrast to atmospheric research deployed satellites, currently balloons allow a variety of in-situ and remote instruments, taking data measurements from the surface to about 1 km, operated at relatively lower cost, thus allowing the recurrence of data measurements over a long period (Pommereau, 2003).

A tethered balloon is a balloon that is restrained by tethers attached to the ground or a platform so it cannot float freely. The base of the tether is wrapped around a winch drum that is used to raise/lower the balloon. Early stages of tethered balloons were a spherical shape in order to use minimal materials. However, in any substantial wind, the balloon shape becomes

aerodynamically unstable and risks damage to the device. In order to combat these issues, the blimp form was developed. Its elongated shape reduces wind resistance and its tail surface allows stabilization in high winds. A hybrid tethered balloon, or kytoon, is specially shaped to provide aerodynamic lift similar to a kite, as well as to reduce drag (Wragg, 2008). Figure 5 below shows a launched balloon attached to a tether.

Figure 5: Launched Balloon (Google Images, 2020)

The sensor package is positioned underneath the kytoon on different lines than the tether line. To capture measurements at different altitudes, the winch is drawn in until the desired altitude is reached. The balloon remains at each altitude of interest to get a statistical sample, before changing its height. Additionally, it can take data measurements while it is changing altitude. In some instances, the sensor package will send its signals down an electrical wire attached to the tether cable. For other kytoons, information is transmitted to the ground station, similarly to radiosondes. However, airspace regulations may restrict deployment to altitudes

below 800 m. Kytoons are very portable and can easily be used at field experiments, but for light to moderate winds only. (Stall, 2009).

1.5 Limitations of Tether Balloons and Kytoons

Although tethered balloons and kytoons have been used frequently in the past for boundary layer analysis to complete ground station measurements, these forms of observation methods are deemed somewhat archaic when compared to new technology. Kytoons are portable and are praised for their mobility but are very susceptible to varying wind movements. This unpredictability of movement can lead to the kytoon sample measurements being skewed easily. The sensors could receive interference from the kytoon in turbulent conditions due to their positioning. Also, a kytoon's payload capabilities would vary based on the size of the balloon and amount of gas needed to reach a certain altitude range. This could create a smaller payload that would be insufficient for carrying sensors to accurately sample within the ABL.

Overall, conventional in-situ observation techniques such as towers, weather balloons types including kytoons, and radiosondes are all somewhat limited in providing adequate sampling within the ABL, and researchers do see data gaps in the meteorological information (Hemingway, 2017). The emergence of UAVs for research purposes has gathered momentum over the last few decades and could potentially change the current course for how in-situ atmospheric data is regularly collected.

1.6 History and Usage of Unmanned Aerial Vehicles

Unmanned Aerial Vehicles (UAVs) or systems provide a versatile, dynamic platform for atmospheric data collection (Hemingway, 2017). UAVs are frequently used by the military and have been a part of many different aspects of research and technology for several decades. Their

use for atmospheric research and other environmental monitoring began in the early 1990s, later becoming commercially accessible in the 2000s. National Oceanic and Atmospheric Administration (NOAA) missions, have routinely used UAVs since 2006 (Axisa, 2016). The Department of Energy (DOE) Atmospheric Radiation Measurement (ARM) Unmanned Aerospace Vehicle (UAV) program was established in 1991 and conducted various field campaigns demonstrating that measurements from UAVs can contribute to our knowledge of cloud and radiative processes. UAVs technology have been shown to be capable of handling the challenges of validating atmospheric data under a large range of natural environments (Axisa, 2016).

Due to the evolving technology of UAVs, they can range in size from 3g to 32,000 lbs and have the capability of a myriad of different payloads depending on the specified mission. The United States Military classifies UAVs into different categories based on their size, gross takeoff weight, and normal operating altitude. The classification can be seen below in Table 1. For this thesis, both UAVs discussed will be in the Group 1 category.

Table 1: US Department of Defense (DoD) Classifications for UAVs

Category	Size	Maximum Gross Takeoff Weight (lbs)	Normal Operating Altitude (ft)	Airspeed (kts)
Group 1	Small	0-20	<1200 Above ground level	<100
Group 2	Medium	21-55	<3500	<250
Group 3	Large	<1320	<18,000	<250
Group 4	Larger	>1320	<18,000 Mean sea level	Any speed
Group 5	Largest	>1320	>18,000	Any speed

UAVs can also be classified into two different types: fixed-wing and rotary-wing. A fixed-wing aircraft consists of a rigid wing with a preset airfoil which generates lift caused by the aircraft's forward speed to create flight. The rotary-wing aircraft differs in the way that it creates

airflow. Its rotor blades work similarly to a fixed-wing aircraft, however constant aircraft forward motion isn't necessary to produce airflow over the blades. Instead, the constant movement of the blades produces the required airflow to generate lift. We will discuss the aerodynamic principles of the two types in more detail in Chapter 3.

Both types of UAVs have advantages and limitations that can greatly affect the atmospheric data sampling within the ABL. UAV technology allows researchers to obtain higher resolution data, reduce the amount of debris contributed by radiosondes, and have a reusable system in place to satisfy the daily need for ABL information that directly contributes to weather prediction. Making measurements using UAVs requires obtaining the necessary permissions from the Federal Aviation Administration (FAA). Current regulations only allow the operation of UAVs within visual line-of-sight up to 365 m (1200ft) above ground level (AGL) in G class airspace. However, as the ABL often exceeds 3 km in depth (or more over some global regions) obtaining information above this 365 m AGL limit is required for UAVs to sample the entire ABL and support weather forecasting operations and agricultural industry needs (Lee T. B., 2019).

Due to its dynamic nature, it is important for UAV researchers and programmers to understand the intralayers and energy exchanges within the transitioning ABL as it progresses throughout the diurnal cycle. Thus, an optimized flight profile can be derived based on desired atmospheric data, the time of day, wind speed, and area roughness. In order to create an optimization process, we need to examine the individual layers of the atmospheric boundary layer in detail.

CHAPTER 2

ATMOSPHERIC BOUNDARY LAYER DYNAMICS

2.1 Atmospheric Boundary Layer Characteristics

Earth's atmospheric boundary layer is complex and constantly shifting, thus creating a fluctuating layer with its unique turbulent flow and interactions with the planetary surface. The ABL is characterized by a diurnal cycle. A diurnal cycle is any pattern that recurs every 24 hours as a result of one full rotation of the Earth on its axis. We can break down the full cycle into various ABL layers based off radiative transfer, evapotranspiration, and stability criteria: the daytime convective boundary layer (CBL) and the nocturnal stable boundary layer (SBL). These ABL subtypes will have sub-zones in them as well such as the capping inversion, surface layer, entrainment layer, and the residual layer.

During fair weather, we are familiarized to the daily changes in temperature, humidity, pollen, and winds governed by boundary layer physics and dynamics (Wallace, 2006). The ABL is typically warm and gusty during the daytime, and cooler and calm at night. The ABL is stated as convectively unstable whenever Earth's planetary surface is warmer than the surrounding air. Examples include a sunlit afternoon with light winds over land, or when cold air is advected over a warm water surface. The unstable boundary layer is in a state of free convection characterized by active thermal updrafts and downdrafts. Conversely, the ABL is considered stable when the planetary surface is colder than the overlying air (Wallace, 2006).

Convection potential energy states are not the only fluctuating properties in the ABL; turbulence plays a main role in boundary layer dynamics. The term turbulence can simply be described as a chaotic or unsteady movement of air, water, or of some other fluid (Wallace,

2006). Wind shear of the mean wind within the boundary layer, that generates from drag near the ground, generates vertical velocity gradients which, in the absence of buoyancy, are the main driver of turbulent flow. Turbulence is also responsible for efficiently dispersing pollutants within the ABL. Turbulent communication between the planetary surface and the air is swift, allowing the air to quickly take on the characteristics of the underlying surface. The ABL will feel the effects of the underlying planetary surface within half an hour or less (Wallace, 2006). Thus, proving the surface layer is an important portion of the ABL that can directly influence boundary layer dynamics and daily life activities on Earth.

2.2 Atmospheric Surface Layer

The surface layer is described as a very shallow region close to the ground; generally depicted as the bottom 10% of the ABL. It is characterized by a super adiabatic lapse rate, strong wind shear, and moisture content profile that decreases with height. Adiabatic lapse rate refers to an atmospheric decrease in temperature as altitude increases. Majority of the wind shear and potential temperature slopes in the ABL are confined in the surface layer. However, surface energy exchanges also play a large role in the surface layer dynamics.

The driving process of the surface energy exchange in the surface layer is a large downward flux of solar radiation, which is absorbed at the Earth's surface during the daytime and is rapidly converted to longwave (IR) heat. While some of the solar heat is transferred down into the surface canopy, the very turbulent nature of the surface layer over the terrain allows a quick upward flux of heat back into the atmosphere. The surface layer is able to avoid huge daily temperature extremes due to this rapid upward flux resulting from turbulence (Geernaert, 2015). However, during the nocturnal boundary layer, the upward flux of IR mixed with nearly no turbulence resulted in colder nights. Higher levels of turbulence present at night provide an

effective mechanism for transferring heat flux quickly down to the surface, resulting in a reduced rate of nighttime cooling (Geernaert, 2015).

Atmospheric properties of humidity, temperature, and wind speed all change swiftly with altitude throughout the ABL's surface layer, but eventually achieve a near constant value with height as they reach the capping inversion. An inversion occurs when the normal temperature lapse rate is reversed, and a stable air configuration is created. However, a capping inversion occurs when the ABL with a normal temperature profile and the layer above that is an inversion layer. Thus, cloud formation from the below layer is "capped" by the inversion layer. As the other atmospheric properties range widely in the surface layer, the wind direction is a relatively constant with the height within the surface layer (Geernaert, 2015). But wind direction can rapidly change direction as height increases, thus its behavior is inverse of the other described atmospheric properties. This directional gradient increase with height is most often due to large scale synoptic conditions (Geernaert, 2015).

In traditional boundary layer sampling, the surface layer tends to be underrepresented in the data due to the lack of sampling time spent in this layer and the strong vertical gradients. In a constant vertical flight path of a UAV, the surface layer will be quickly exited within the first few seconds of flight and not returned to until the flight has almost concluded. Thus, the majority of data gathering occurs within the mixing regions of the ABL if the UAV has a constant rate of climb. Adequate data sampling of the surface layer is essential to accurately establish the flux profile and turbulence levels in the ABL. These values will set the tone of the resulting layers above in the ABL and play a large role in determining the aerodynamic roughness length. The aerodynamic roughness length is a length scale that represents the roughness of the surface. This

value can then be used to estimate mixing lengths for eddies within the ABL. This concept is further expanded on in Chapter 5.

2.3 Entrainment Layer

The very nature of the ABL depends on the stability structure of the air parcels within each layer. The capping inversion located at the top of the ABL is not a solid boundary. Thus, when thermal plumes and eddies from the convection boundary layer (or mixed layer) reach the capping inversion, their inertia forces them to overshoot slightly into the capping inversion before descending down into the CBL. During this overextension, the air inside these eddies and thermals has temporary left the CBL, and the pressure gradient created by this drives parcels of free tropospheric air downward into the mixed layer (Wallace, 2006). These parcels of free air that entered the CBL are immediately torn and mixed due to the strong turbulence within the layer. The air parcels will assimilate into the CBL and will never rise back up to the free atmosphere. This entire process is depicted as entrainment and occurs in the entrainment zone of the ABL.

Entrainment is a one-way process that adds air mass from a non-turbulent region into the turbulent mixed layer. As the sun rises, the heat from solar radiation within the surface layer warms the surrounding air which creates shallow thermals that rise and eventually mix. Essentially, the convective boundary layer gradually eats its way up into the overlaying air, thus placing the entrainment layer at the top of the ABL parallel to the capping inversion (Wallace, 2006). The entrainment will evolve throughout the day and eventually will become the new capping inversion of the ABL as it takes over the previous capping inversion. However, when sunset approaches, the ABL transitions into the nocturnal stable boundary layer (SBL) which has a completely different dynamic structure.

The CBL is not a closed system with a fixed mass per area, thus the entrained air volume above it increases or decreases in response to large-scale vertical velocities present within the ABL. An increase of turbulence in the convective layer causes more powerful entrainments. However, if a strong capping inversion in present, entrainment will be reduced due to minimal inertia overshoot (Wallace, 2006). Sensible heat flux generated from the surface layer also plays a role in determining the strengthening rate of the entrainment zone. There are many variables affecting the CBL, and the majority of vertical profiles of these properties increase or decrease while going through all the individual layers of the boundary layer. Figure 6 below shows a graphical representation of vertical properties in the CBL and how the profiles change in terms of each layer.

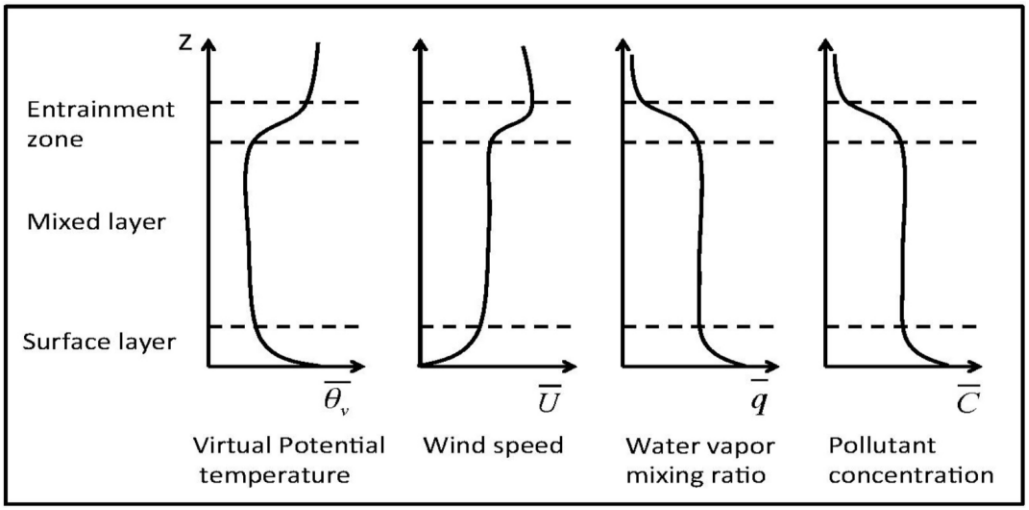

Figure 6: Vertical profiles of average variables in Convective Boundary Layer (Stall, 2009)

2.4 Residual Layer

As the convective boundary layer evolves with the diurnal solar input, it eventually reaches a point where it transitions into the stable nocturnal boundary layer (SBL). The nocturnal boundary layer can be denoted as the stably stratified shallow boundary layer hovering right above the ground. With this evolution comes the creation of a new layer within the ABL, the residual layer. The American Meteorological Society (AMS) describes the residual layer as the "…middle portion of the nocturnal boundary layer characterized by weak sporadic turbulence and initially mixed potential temperature and pollutants remaining from the mixed layer of the previous day." The capping inversion remains in its same position, placed above the residual layer separating from the free atmosphere air described in the entrainment layer section.

The rising thermals characterized in the CBL cease once the sun sets, causing the turbulence in the residual layer to become stagnant. Direct reduction in the surface heat flux leads a lack of turbulence due to less vertical mixing (Wingo, 2014). Atmospheric scientists often focus on the residual moisture, heat and pollutant variables trapped within the stable layer. These variables can greatly affect the next day's CBL as well as the formation of fog or frost which is important to the agriculture industry. Also, an adequate sampling of the residual layer can provide additional information on the concentration of pollutants in the ABL. This is important to monitor for many different industries, including but not limited to forest management, transportation safety and public health (Wingo, 2014). Figure 7 below illustrates how vertical profiles temperature gradients change as the ABL transitions through its diurnal cycle.

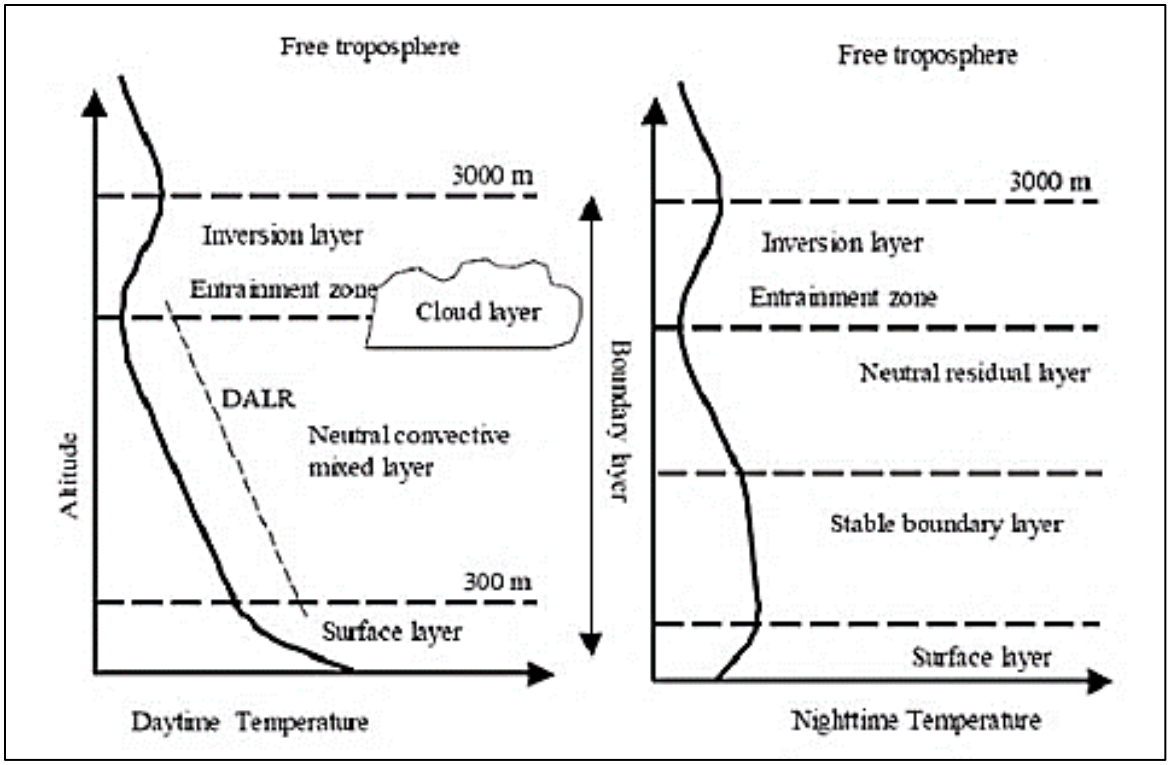

Figure 7: Vertical profiles of temperature gradients throughout the ABL (Stall, 2009)

2.5 Nocturnal Boundary Layer

As introduced before, the stable nocturnal boundary layer is located directly between the surface layer and residual layers formed during the nighttime portion of the ABL diurnal cycle. The American Meteorological Society (AMS) denotes the stable nocturnal boundary layer as "…a cool layer of air adjacent to a cold surface of the Earth, where the temperature within that layer is statically stable stratified." Sporadic turbulence, buoyancy, drainage flows, inertial oscillations and nocturnal jets are all interacting processes that occur in the SBL. This layer is deemed to be more stable than its above residual layer, however both layers share similar characteristics in terms of turbulence. The loss of heat flux and surface cooling in both layers directly correlates to the diminishing turbulence values.

In early evening transitions to the SBL, there is a sharp increase in specific humidity and a rapidly decrease in surface temperature just before sunset. Wind gusts decline in magnitude, which is an indication of decaying turbulence in the surface layer. During the transition to the nocturnal stage, the sensible heat flux at the surface is often negative while the latent heat flux is positive and upwards (Bonin, 2012). Stability is the overarching characteristic of the ABL during the nighttime period. It is vital to sample the processes within the SBL to accurately provide forecasting data to the NWS.

A study completed at the Max Planck Institute for Meteorology in Hamburg, Germany (Stratum, 2015), addressed the question: How accurately must the nocturnal boundary be sampled in order to acquire a reliable representation of the daytime convection? In a series of numerical experiments, an underestimation of the SBL depth and turbulence values led to an under representation of ABL temperature during the next day's daytime convection (Stratum, 2015). Thus, demonstrating that adequate sampling within the stable nocturnal boundary layer plays a key position in fully characterizing the atmospheric boundary layer.

2.6 Boundary Layer Stages and their effects on UAV Flight and Data Collection

The ABL is always transitioning throughout its diurnal cycle which makes boundary layer research challenging and complex. However, it is important to characterize all transition periods and layers within the diurnal cycle. Due to the consistent evolution of layers within the transitional periods, it is imperative that observational UAV flight missions are tailored to each layer's height to achieve a sufficient amount of sampling among the layers. Traditional radiosondes, balloons, and radar towers cannot provide an individualized rate of climb. UAVs are the next technology step that can bridge the gap of the misrepresented information within the ABL, and in turn can directly help with accurate forecasting. However, in order to correctly

sample the layers within the ABL, UAV flight profiles must be adapted accordingly based off the depths and characteristics of each intralayer.

Current UAV vertical flights with constant ascent rate will potentially under sample the lower atmospheric layers, thus oversampling the layers at the top. Additionally, by the time the UAV returns to the ground, the boundary layer has evolved into a completely different structure than at the original take off time. In this thesis, it was proposed to create step flight profiles to optimize data sampling within the ABL at the time of each flight. Each flight path optimization denotes the present layers during the sampling timeframe, estimate the individual layer's depth, and create a series of horizontal and vertical steps to allow enough time for sensors to evenly capture data among the transitioning layers during both the daytime and nighttime portions of the ABL diurnal cycle.

As previously stated, UAVs can be classified into two different types, fixed-wing and rotary-wing, and each comes with advantages and limitations for flight path optimizations. In the following chapter, we will discuss the aircrafts used for this thesis as well as the aerodynamic parameters that must be accounted for in the optimization process.

CHAPTER 3

AERODYNAMIC PRINCIPLES OF FIXED-WING AND ROTARY-WING UAVs

3.1 Introduction to Aerodynamic Parameters

UAV technology allows researchers to obtain higher resolution data, reduce the amount of ground debris waste by radiosondes, and have a reusable system in place to satisfy the daily need for ABL information that directly contributes to weather forecasting. Both fixed-wing and rotary-wing types of UAVs have advantages and limitations that can greatly affect the atmospheric data sampling within the ABL. As previously mentioned, a fixed-wing aircraft consists of a rigid wing with a predetermined airfoil which makes flight capable by generating lift caused by the aircraft's forward speed. The rotary-wing aircraft uses the constant movement of the blades to produce the required airflow to generate lift. Despite the differing sources in airflow generation, both unmanned aircraft types can be characterized with aerodynamic principles.

Aerodynamic properties are vital to understanding the parameters in which one's aircraft can operate. Endurance, range, rate of climb, drag and lift coefficients are among the most important values to determine for flight optimization. Once calculated, we can reasonably estimate the performance we will see from the UAV during its flight, as well as help determine which wing type of UAV is optimal for the necessary mission. Using the following formulas (Asselin, 1997), we can evaluate the aerodynamic properties for both the fixed-wing, BlackSwift S2, and the rotary-wing, Meteomatics Meteodrone, used for this study.

In order to calculate the desired parameters, the vehicle characteristics must be defined. These characteristics include the maximum takeoff weight, maximum payload allowance, wing

span, wing reference area, span efficiency (Oswald efficiency), and battery power available. Assuming steady flight, all forces are in equilibrium, and standard atmospheric conditions, we can calculate the various lift and drag coefficients acting on the aircraft at different speeds.

$$A = \frac{b^2}{S} \tag{1}$$

$$L = C_L\left(\frac{\rho}{2}\right) \times V^2 \times S \tag{2}$$

$$D = C_D\left(\frac{\rho}{2}\right) \times V^2 \times S \tag{3}$$

$$C_L = \left(\frac{W}{S}\right)\left(\frac{2}{\rho}\right)\left(\frac{1}{V^2}\right) \tag{4}$$

$$C_D = C_{D0} + C_{Di} = C_{D0} + (K \times C_L^2) \tag{5}$$

$$C_{Di} = \frac{C_L^2}{\pi \times A \times e} \tag{6}$$

$$K = \frac{1}{\pi \times A \times e} \tag{7}$$

Lift and drag coefficients are evaluated at all different flight speeds in order to characterize the aircraft during its climbing and cruising altitude stages. When an aircraft is going from one velocity to another, its conditions become unbalanced briefly but return to a balanced state once steady flight is achieved. Steady level flight is denoted as the state in which the aircraft's thrust is equal to its drag and its lift is equal to its weight. During the climbing or descending portions of flight, the lift equations change depending on the climb angle. The angle of attack parameter is important in determining lift during steady state flight as well as climb performance. The angle of attack (α) can be described as the angle between the plane of the wing (airfoil chord) and the direct free stream of velocity from the relative wind (Asselin, 1997). If an

aircraft's angle of attack is 0 degrees, then its lift is zero. Additionally, minimum drag coefficient also occurs at zero lift, thus proving how all the various lift and drag coefficients heavily rely on each other to properly calculate an aircraft's lift and drag moments throughout its flight. Angle of attack values along with lift coefficients can also help calculate vital aircraft velocities: stall speed, optimal cruising speed, and maximum flight speed. However, it is important to note the following equations are designed for symmetric airfoils. If the aircraft in question does not have a symmetric airfoil, a specific airfoil information pertaining to the angle of attack must be measured in a non-empirical fashion.

$$\alpha = \frac{C_L}{\pi \times A} \tag{8}$$

$$C_{L\alpha} = \frac{dC_L}{d\alpha} = 2\pi \times \left(\frac{A}{A+2}\right) \tag{9}$$

$$L = W \times \cos(\gamma) \tag{10}$$

From these calculated values, we can now determine the unmanned aircraft's flight range, flight endurance, and rate of climb. In aerodynamics, a lift-to-drag ratio (L/D ratio) can be denoted as the amount of lift generated divided by an aircraft by the drag it creates moving through the air. A higher L/D ratio is especially favorable in aircraft design due to this ratio providing a lift with lower drag that leads to better fuel economy, climb performance and glide ratio (Asselin, 1997). L/D ratios can be derived at both the cruising speed and the climbing speed in order to optimize the aircraft during both portions of its flight. The flight path angle (FPA) or angle of climb has a different definition. It can be described as the angle between the aircraft's velocity vector and the local horizontal with respect to the Earth's surface. From these recorded values, the rate of climb (ROC), of the aircraft can be calculated. Once the ROC is computed,

subsequent values such as the specific excess thrust, and specific excess power can be calculated. The climb angle (γ), is directly proportional to the specific excess thrust over the aircraft weight value, while the climb rate is proportional to the specific excess power. In order to accurately understand an aircraft's level climb properties, it is known that the maximum angle of climb occurs at the maximum excess thrust. Similarly, the maximum rate of climb occurs at the maximum excess power.

Another vital parameter that can shape flight range and endurance values, is the propulsive efficiency. This is an ideal efficiency that characterizes by the product of the vicious profile drag on an aircraft's blades and the kinetic energy lost. It can also be calculated by using the thrust developed and the power generated by the engine shaft. When calculating propulsive efficiency, it is important to understand the aircraft's power source and whether it is categorized as a propeller or jet engine vehicle. An aircraft with a propeller has a constant power, whereas a jet aircraft has constant thrust. For the UAVs used in this study, the propulsive efficiency can be calculated based off the power wattage provided by the installed batteries.

$$\eta_P = \eta_o \times \eta_i = \frac{(T \times V)}{P_e} \tag{11}$$

$$T(V) = \eta_P \times P_e \tag{12}$$

$$\left(\frac{L}{D}\right) = \frac{1}{2}\sqrt{\frac{\pi \times A \times e}{C_{D0}}} \tag{13}$$

$$R = \frac{\eta_P}{C_{ps}} \times \left(\frac{L}{D}\right) \times \ln\left(\frac{W_{initial}}{W_{final}}\right) \tag{14}$$

$$E = \frac{\eta_P}{C_{ps}} \times \left(\frac{L}{D * V}\right) \times \ln\left(\frac{W_{initial}}{W_{final}}\right) \tag{15}$$

$$ROC = \frac{dH}{dt} = V \times \sin(\gamma) \tag{16}$$

$$ROC = \frac{P_{av} - P_{req}}{W} \tag{17}$$

By calculating these aerodynamic parameters with the equations above, we can interpret the mission capabilities of each UAV and further optimize our flight plans based off the optimal cruising speeds and the L/D ratios. Understanding the aerodynamic principles behind fixed-wing and rotary-wing aircrafts directly correlates to flight path optimization. By conceptualizing the aircraft's flight dynamics, we can confidently create a flight path to ensure each stage within the atmospheric boundary layer can be adequately sampled without fearing of stalling the UAV or facing a limited maximum endurance. In Table 2 below, the aerodynamic parameters for both the BlackSwift S2 and the Meteomatics Meteodrone are displayed.

Table 2: Aerodynamic Parameters for UAVs

Parameter	BlackSwift S2 Fixed-Wing UAV	Meteomatics Meteodrone SSE Rotary-Wing UAV
Wing Span	3.0 m (10 ft)	0.6 m (2 ft)
Length	2.0 m (6.5 ft)	0.6 m (2 ft)
Takeoff Weight	5.2 kg (11.5 lbs)	0.7 kg (1.5 lbs)
Max Weight	6.6 kg (14.5 lbs)	0.77 kg (1.7 lbs)
Payload Weight	2.3 kg (5 lbs)	0.2 kg (0.5 lbs)
Engine Type	1 Electric Motor	6 Electric Motors
Power Available	50 watts	47.7 watts
Endurance	1.83 hours (6600 seconds)	0.2 hours (720 seconds)
Range	110 km (60 nm)	14.4 km (7.8 nm)
Cruise Speed	18 m/s (35 kts)	3 m/s (6 kts)
Stall Speed	12 m/s (24 kts)	N/A
Max Speed	24.7 m/s (48 kts)	20 m/s (39 kts)
Max Altitude	6000 m (20,000 ft)	1500 m (5,000 ft)
Max Rate of Climb	22 m/s (43 kts)	19 m/s (37 kts)

3.2 General Fixed-Wing UAV Dynamics

Fixed-wing UAVs consist of a rigid wing with a predetermined airfoil which makes flight capable by generating lift caused by the aircraft's forward speed. This lift change results from an increase or decrease of its angle of attack (α). Gliding fixed-wing aircrafts use moving air within the atmosphere to gain altitude, while powered fixed-wing aircraft gain forward thrust (Asselin, 1997). The structural components of a fixed-wing aircraft are referred to as the airframe. The airframe includes horizontal wings, fuselage, vertical stabilizer, horizontal stabilizer, and landing gear.

When designing an airframe, the three angles of flight rotation (pitch, roll and yaw) are critical. These angles of rotation occur around the aircraft's center of gravity, commonly referred to as cg, during the steady state flight. Roll is defined as the rotation acting about the longitudinal axis. When an aircraft's wings are level, this is denoted as the equilibrium roll angle. The dihedral wings on a fixed-wing aircraft provide stability in roll to stop the aircraft from dipping the wings during steady state flight. Yaw is the rotation acting about the aircraft's vertical body axis. The vertical stabilizer, or fin mounted at the rear of the aircraft, steadies the yaw. Lastly, pitch is the rotation acting about the axis perpendicular to the longitudinal plane of symmetry. The horizontal stabilizer, also mounted in the rear, controls the aircraft's pitch (Asselin, 1997). Figure 8 shows the angles of flight rotation on a fixed-wing aircraft in flight. The pitching moment directly correlates to the angle of attack measure that governs lift. To increase the angle of attack during takeoff, an aircraft pitches nose up. Too much pitch will greatly slow the aircraft's speed causing a stall pattern in flight.

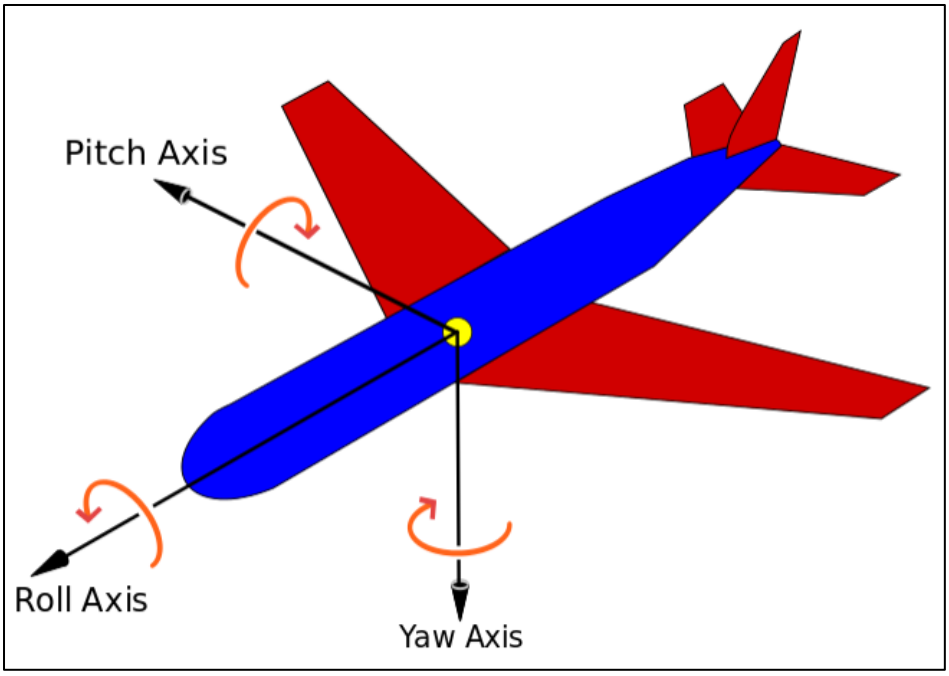

Figure 8: Flight Angles of Rotation (Google Images, 2020)

3.3 Advantages and Limitations of Fixed-Wing UAVs

The fixed-wing UAV design offers the additional benefits of having a larger payload capability, longer endurance, higher flight ceiling, and a greater range when compared to its rotary-wing counterpart. The wing structure is solely responsible for the aircraft's lift production, resulting in reliable lift and drag values during flight (Panagiotou, 2019). These set values allow for steady state flight to be easily achieved and clear stall, cruise, and maximum speeds to be calculated prior to flight. The fixed wingspan also contributes to greater flight ceilings, endurance and range values. Thus, enabling fixed-wing UAVs to capture larger survey areas. Fixed-wing aircraft can also assume gliding flight without the use of the main motor. If the UAV power becomes limited, the fixed-wing aircraft can glide, which can greatly help in battery management.

Additionally, the ability to have a larger airframe allows for a higher payload capability, which is vital for atmospheric research sensors. Observation projects often require different atmospheric sensors to be stored within the payload of a UAV. A larger payload or even an ability to interchange the sensors is very beneficial. A more rigid airframe also allows UAVs to be able to fly in extreme environments and are less susceptible to winds during flight. Also, the simpler airframe structure provides less complicated maintenance if needed. Fixed-wing UAVs are viewed as a durable option for researching purposes when compared to rotary-wing aircrafts, but there are limitations with this type too.

Fixed-wing aircrafts require a large takeoff and landing area. Fixed-wing UAVs need a proper runway or catapult to reach the required velocity to lift into the atmosphere. Thus, research areas need to be accommodated with a clear space in order to accurately operate a fixed-wing UAV (Boon, 2017). The unpredictability of crosswind effects in the atmosphere boundary layer can also complicate final landing approaches. Crosswind effects can be denoted as the wind gusts and turbulence occurring during approach to landing. Pilots and autopilots have methods in place to combat landings in adverse weather effects, however it should be noted that this is also another limitation fixed-wing UAVs face (Bruin, 2016).

Also, a fixed-wing UAV cannot “hover” in flight like a rotary-wing UAV. In order to achieve near vertical flight, a fixed-wing aircraft must perform a spiral flight maneuver to characterize an area while rising in altitude. This presents a difficulty when trying to capture multiple vertical atmospheric profiles over a set altitude range. Flight planning involving fixed-wing UAVs requires a larger timeframe, so multiple flights over an observation area could take up over double the time needed when compared to a rotary-wing UAV in the same area. Each

research study is different and entails certain flight expectations, so unmanned aircraft must be selected on a case-by-case basis.

3.4 BlackSwift Technologies S2 UAV Characteristics

The BlackSwift S2 is a fixed-wing unmanned aircraft that was purposely manufactured for flying scientific payloads in demanding atmospheric environments. It is engineered to withstand corrosive particulates, strong turbulence, and achieve high altitude in complex terrain systems. This aircraft is designed with the capability to either be hand-launchable or launched via rail system. Its engine type is an electric motor fueled by a set of rechargeable lithium polymer battery cells. The payload for this particular model is located in the nose cone (8 in diameter, 24.9 in length). It can be equipped with sensors to measure air temperature, humidity, pressure via iMet XQ-2 sensor, and surface temperature and imaging via TeAx ThermalFusion visible and infrared camera (Lee T. B., 2019). For this study, only the temperature and humidity sensors are vital for flight path optimizations within the ABL.

BlackSwift has developed a flight planning user interface that allows the S2 technician to program the aircraft to calculate the area under review and begin collecting data in real time for field analysis. The S2 mission monitoring and mapping is controlled via handheld tablet. The launching rail is a large steel frame with a pneumatic automated catapult system. Figure 9 below shows the BlackSwift S2 UAV.

Figure 9: BlackSwift S2 in Oliver Springs, TN

3.5 General Rotary-Wing UAV Dynamics

Rotary-wing flight is also governed by the three angles of flight rotation: pitch, roll and yaw. However, the lift generation differs from its fixed-wing counterpart. Instead of a rigid wing with a predetermined airfoil, rotary-wing UAVs consist of multiple blades that revolve around the fixed mast, referred to as the rotor. Rotary airframe styles can range from one rotor to 8 (octocopter) or more rotors depending on the flight specifications. Rotary-wing aircraft use the constant movement of the blades to produce the required airflow to generate lift. However, the angle of attack (α) does slightly differ from the fixed-wing aircraft design. On the rotary-wing style, the angle of attack is the angle between the airfoil chord line and relative wind. Rotary-wing UAV pilots have discovered that numerous factors can change the rotor blades' angle of attack. Some of these outside factors can be mitigated but other factors occur naturally due to the

inherent rotor system design. This continual change in the angle of attack accommodates rotary-wing flight and is an integral part of travel of the rotor blade through the rotor disk. However, pilots do not have control over blade flapping/flexing due to turbulent air conditions (Rotaru, 2018).

The basic flight regimes of a helicopter include hover, climb, descent and forward flight. During these different stages of flight, the rotary-wing aircraft flight dynamics can be explained by actuator disk theory. This theory is a mathematical model of inducing constant velocity along the axis of rotation on an ideal actuator disc, in this case the UAV's rotors. The disc creates a flow around the rotor, and the power required to generate a given thrust is found (Rotaru, 2018). In a hover situation, the air velocity is null and the ideal power requirement to hover is met. The thrust force is also normalized, similar to fixed-wing aircraft, and is a product of the pressure at the rotor blade disc and total disc area. Both hovering and vertical climb conditions can be described using similar dynamic approaches, but descent rate conditions pose a more complex issue (Rotaru, 2018). For this particular study, only hovering and vertical climb flight dynamics are essential for profile optimizations within in ABL. Figure 10 demonstrates the dynamic forces, angle of attack and planes of rotation enacting on the rotary blades and main rotor mast during flight.

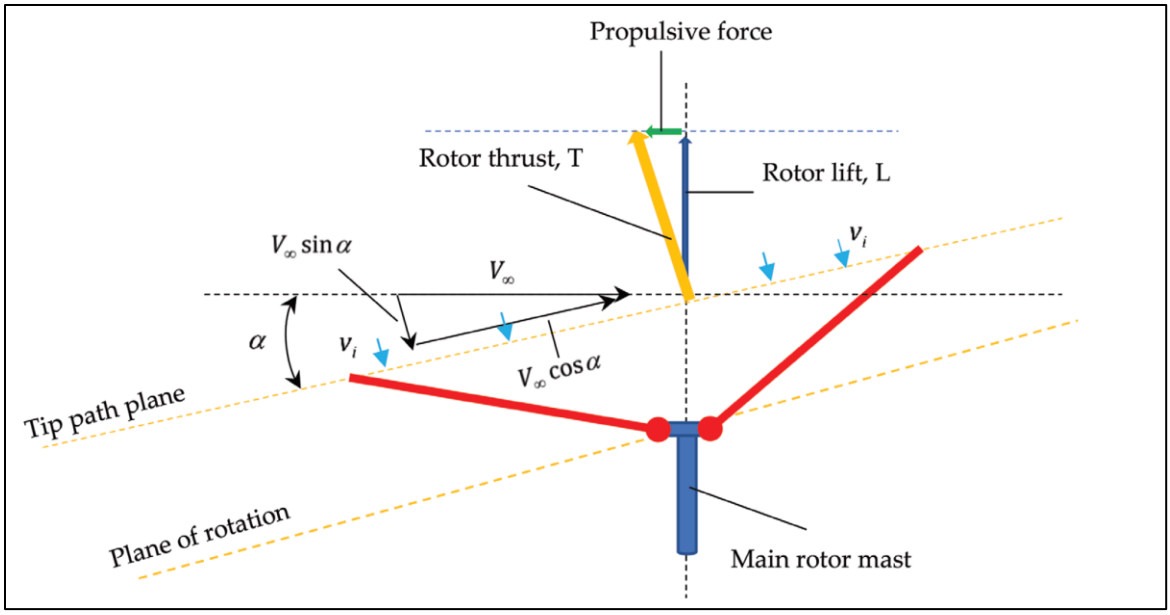

Figure 10: Aerodynamic Parameters on Rotor in Flight (Rotaru, 2018)

As previously mentioned, pitch, roll and yaw do play an important part in rotary-wing stability conditions. Control of the UAV comes from the variation in thrust and torque produced by the rotors. In a multi-rotor UAV, downward pitching moment is generated by the back rotors producing more thrust than the front, thus creating a nose down flight pattern. For yaw motion, the rotor's torque force in the diagonal rotors more than the counter rotors causing an imbalance in the yaw rotation axis. The roll axis is connected to the yaw axis, like in fixed-wing aircraft. Therefore, yaw and roll are referred to as one lateral movement for rotary-wing aircraft (Rotaru, 2018). However, it is noted that rotary-wing aircraft are estimated to have 50% of the endurance of fixed-wing aircraft of the same weight with a moderate L/D ratio (Prudden, 2018). An increased power required to generate thrust via rotors directly results in lowered endurance values. Flight control systems for rotary-wing unmanned aircraft are managed from a ground-based pilot via remote controllers or are pre-programmed.

Rotary-wing aircraft have the ability to participate in autorotation. Autorotation is denoted as a state of flight in which the main rotor system turns by moving up air through its rotor, rather than having traditional engine power. Autorotation provides the pilot with alternate power situations to attempt to increase the aircraft's range and endurance. This action is analogous to gliding flight of fixed-wing aircraft previously mentioned. Autorotation can also be used in situations of limited power supply and/or total engine failure. As the rotary-wing aircraft falls in altitude, the air rushes up from under the main rotor. This rushing air in turn pushes the blades, thus turning the rotor without any provided power. Also, in certain altitude cases, autorotation may also be used to recover from the hazardous vortex ring state (Rotaru, 2018).

Vortex ring state is a dangerous flight condition that overwhelms the rotor causing a severe loss of lift (Rotaru, 2018). Also, referred to as "Settling with Power", this condition arises from a disturbance in proper airflow around the main rotor. When vertical descent rate increases to a prescribed value, an up flow of air begins because there are no airfoil surfaces in the mast or the blade grip area. As the volume of the up flow increases, this same air is pulled through the rotor (induced flow) and results in a dramatic loss of lift given the power setting. The vortex ring state must be avoided as it could cause the rotary-wing UAV to descend at a high rate or even have ground impact. Alternatively, it takes roughly twice the normal hover power to attempt to power out of a vortex ring state (Rotaru, 2018). Because of the vortex ring state, not every descent rate is possible, and particular vortex ring states (a combination of power and descent rate) for every particular rotary-wing unmanned aircraft must be avoided in our flight optimizations.

3.6 Advantages and Limitations of Rotary-Wing UAVs

The rotary-wing UAV design offers the additional benefits of agile in flight maneuvering, hovering capabilities, and vertical takeoff/landings when compared to its fixed-wing counterpart. These UAVs can also be programmed to perform simple vertical profiling flights in areas with limited runway space. The ease of a simple vertical takeoff procedure is a strong advantage over fixed-wing models that require either a pneumatic launch system or a cleared runway. This creates an opportunity to fly in complex terrain and even in close proximity to structures. Specifically, multi-rotor unmanned aircraft systems have gained popularity over the last few years due to fundamental robustness, affordability and compactness (Prudden, 2018). Multi-rotor UAVs have fixed pitch rotors that operate at variable rotational velocity allowing the aircraft to make agile movements in the atmosphere. This ability attributes to excellent stability and control in the rotational axes: pitch, roll and yaw.

However, rotary-wing aircraft tend to survey smaller surface areas than traditional fixed-wing aircraft and also have poorer endurance and range abilities (Boon, 2017). As briefly mentioned, there is a maximum endurance and range trade off in order to supply the rotors with enough power to generate thrust during flight. Limited payload capacity also is a disadvantage when compared to the fuselages on fixed-wing aircraft. This constrained space can create a weight conflict when installing specific sensors. Rotary-wing UAVs can have more complex electrical systems which if malfunctioning can require complicated maintenance and lengthy repair times.

Also, rotary-wing UAVs tend to be smaller in overall size, thus making the aircraft susceptible to horizontal wind gusts. Turbulence can change the angle of attack of the blades and induce unsuspected movements (Prudden, 2018). In a study conducted by the National Center of

Atmospheric Research (NCAR), small rotary-winged UAVs flying at relatively low airspeeds are more sensitive to small-scale wind structures, especially vertical wind (Cornman, 1995). In order to combat this, the rotary-wing UAV has an immediate vertical acceleration response which can potentially disrupt atmospheric sampling if a specific altitude and hold time is required.

3.7 Meteomatics Meteodrone SSE UAV Characteristics

The Meteomatics Meteodrone SSE is a multi-rotor unmanned aircraft that was built to collect highly precise measurements of temperature, humidity and windspeed within the planetary boundary layer. Due to its low weight and powerful motors, this model is able to operate in extreme weather conditions and high turbulence. Its hexacopter build allows vertical flight at a rapid speed as well as vertical takeoff and landings. The Meteodrone SSE can be placed on any ground for immediate takeoff once the system is powered up. Its engine type is an electric motor fueled by a set of rechargeable lithium polymer battery cells, similar to the BlackSwift S2. It is equipped with sensors to measure air temperature, humidity, and wind speed and direction. It is also equipped with strobe lights visible during daylight to keep constant sight on the UAV.

Mission monitoring and mapping is controlled via ground station and remote control. Using the collected atmospheric values, Meteomatics uses a patented program to generate temporal profiles of selected weather parameters for a deeper explanation of the ABL at time of flight. These include dew point, relative humidity, temperature, mixing ratio, pressure, wind speed and wind direction plots. Figure 11 shows the Meteomatics Meteodrone SSE UAV.

Figure 11: Meteomatics Meteodrone SSE (Meteomatics, 2020)

CHAPTER 4

RESULTS OF FLIGHT TEST EXPERIMENT

4.1 Experiment Background

During March 4th to 6th 2019, a team from NOAA Air Resources Lab (ARL) Atmospheric Turbulence and Diffusion Division (ATDD) conducted an experiment that included multiple flights completed with both BlackSwift S2 and Meteomatics Meteodrone SSE aircraft. The experiment occurred in Avon Park, Florida, a U.S. Air Force test range 100 km south of Orlando, Florida (Lee T. B., 2019). The team consisted of members from ATDD, NOAA's Unmanned Aircraft Systems Program Office, and NOAA's Office of Marine and Aviation Operations Aircraft Center. Avon Park sits 20 meters above sea level. Weather conditions were normal during the observation period.

The experiment was conducted to demonstrate the abilities of both unmanned aircrafts as viable options for boundary layer research. Additionally, it also served as an opportunity to fly the aircraft at higher altitudes which would allow the data captured to support operational weather forecasting. Due to Avon Park's specific purposes, the airspace is not governed by normal FAA regulations, allowing for the UAV to be piloted at maximum altitudes of 1500 m (5000 ft) above ground level (AGL). A ground-based radar system was also employed for this experiment to mitigate possible threats to the UAVs in the airspace during flight. These threats can include, but are not limited to, traditional aircraft, birds, other unmanned aircraft, balloons, etc. (Lee T. B., 2019).

The experiment data collected is vital to this thesis for the comparison of the temperature and relative humidity data captured by each aircraft. Additionally, data captured by NOAA

showed a strong need optimized flight paths for ABL research in replacement of free or tethered balloons. This data was used to create the flight path optimizations discussed in Chapter 5.

4.2 Flight Plans

During the 3 day observation period, 17 vertical flight profiles were completed with the Meteodrone SSE, and 7 flights were completed with the BlackSwift S2. The Meteodrone performed vertical takeoff and landing (VTOL) flights with a fixed rate of climb. The aircraft was flown to a maximum altitude of 950 m (3117 ft) during one of its flights. For all flights, the Meteodrone was equipped with sensors to measure air temperature, humidity, and wind speed and direction. Table 3 below displays flight dates, flight type, take off time (UTC), landing time (UTC), and flight duration for the Meteodrone SSE.

Table 3: Avon Park Experiment Meteodrone SSE Flight Timetable (Lee T. D., 2019)

Date	Flight Type & Number	Flight Start Time	Flight End Time	Flight Duration
March 4	VTOL (1)	14:24	14:32	8 mins
March 4	VTOL (2)	15:12	15:18	6 mins
March 4	VTOL (3)	15:43	15:49	6 mins
March 4	VTOL (4)	16:05	16:10	5 mins
March 5	VTOL (5)	20:29	20:35	6 mins
March 5	VTOL (6)	20:43	20:49	6 mins
March 6	VTOL (7)	14:10	14:15	5 mins
March 6	VTOL (8)	14:22	14:27	5 mins
March 6	VTOL (9)	14:34	14:38	4 mins
March 6	VTOL (10)	14:42	14:47	5 mins
March 6	VTOL (11)	14:56	15:01	5 mins
March 6	VTOL (12)	20:23	20:28	5 mins
March 6	VTOL (13)	20:34	20:41	7 mins
March 6	VTOL (14)	20:46	20:53	7 mins
March 6	VTOL (15)	20:57	21:06	9 mins
March 6	VTOL (16)	21:10	21:17	7 mins
March 6	VTOL (17)	21:24	21:36	12 mins

The BlackSwift S2 was launched using the launching rail in an area approximately 80 m (262 ft) east of the Meteodrone vertical takeoff location. Using the spiral flight maneuver with a diameter of 100 m (328 ft), the S2 reached a maximum altitude of 1200 m (3937 ft) during one of its flights. For all flights, the S2 was equipped with sensors to measure air temperature, humidity, pressure via iMet XQ-2 sensor, and surface temperature and imaging via TeAx ThermalFusion visible and infrared camera. Table 4 below displays flight dates, flight type, take off time (UTC), landing time (UTC), and flight duration for the S2.

Additionally, the S2 was also flown in lawnmower-type flight maneuvers in order to characterize the spatial variability of temperature, moisture, and thermal characteristics of the land surface. These flights are the 6th and 7th flights conducted on March 6th in Table 4 below. However, for this thesis, only data from the intercomparable flights (S2: 1-5) were of interest.

Table 4: Avon Park Experiment S2 Flight Timetable (Lee T. D., 2019)

Date	Flight Type & Number	Flight Start Time	Flight End Time	Flight Duration
March 4	Spiral Flight (1)	19:14	19:28	14 mins
March 4	Spiral Flight (2)	20:01	20:17	16 mins
March 4	Spiral Flight (3)	20:32	20:59	27 mins
March 5	Spiral Flight (4)	20:16	20:52	36 mins
March 5	Spiral Flight (5)	21:08	21:59	51 mins
March 6	Lawnmower Flight (6)	19:03	19:37	34 mins
March 6	Lawnmower Flight (7)	20:32	21:07	35 mins

4.3 Intercomparison Results

From the data sampled on the March 5th flights, the air temperature and dew point temperature measurements from the Meteodrone SSE were compared to the air temperature, moisture and pressure measurements captured by the iMet XQ-2 sensor on the BlackSwift S2. The sensor uncertainty for the Meteodrone SSE is ± 0.1 °C for temperature and ± 0.2 °C for

humidity. Sensor uncertainty for the BlackSwift S2 is ± 0.5 °C on both temperature and humidity. Overall, the sensors showed good agreement. Temperatures captured by both aircraft agreed to ± 0.2 °C margin. However, dew point temperatures were not as precise with 0.5 °C higher captured from the Meteodrone SSE when compared to the S2 measurements. Figure 12 shows the temperature and the dew point temperature comparisons of both aircraft. The Meteodrone is represented by the red data points whereas the S2 is represented by the blue (Lee T. B., 2019).

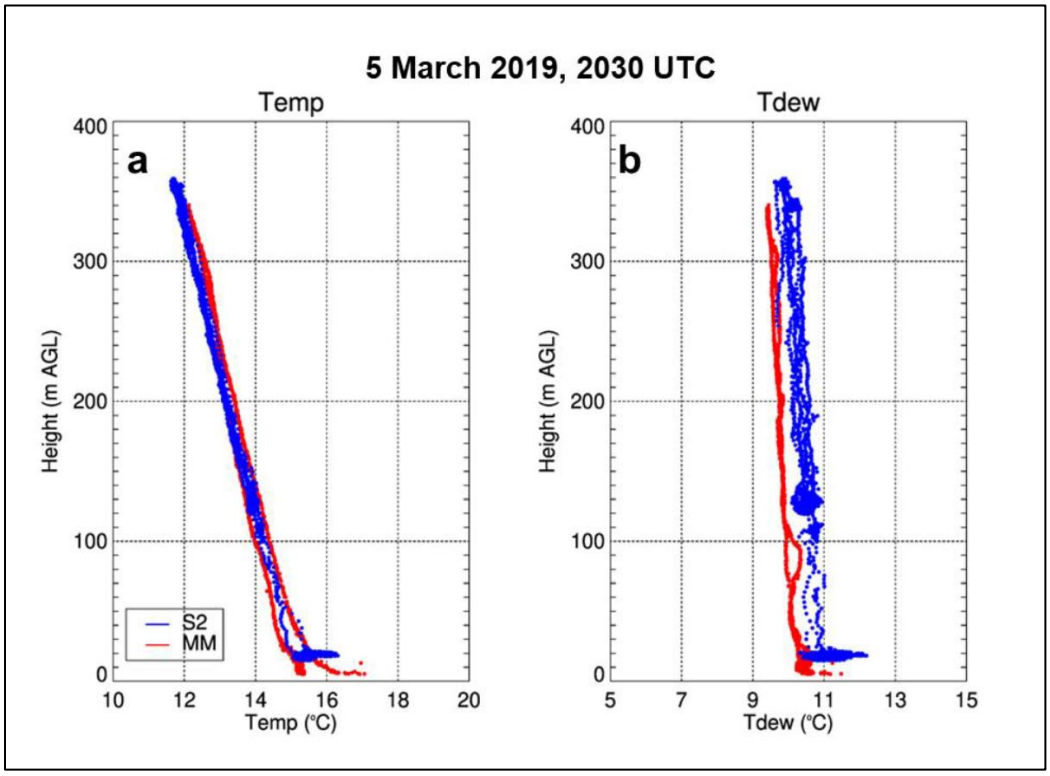

Figure 12: Temperature (left) and the Dew Point Temperature (right) of Meteodrone SSE & S2 (Lee T. B., 2019)

Due to the sensors capturing congruent data, we can confidently state that either the fixed-wing BlackSwift S2 or rotary-wing Meteomatics Meteodrone SSE can be used for adequate data collection of atmospheric values in the boundary layer. The two aircraft were

flown at the same time over a 20:16 UTC to 21:59 UTC timeframe to ensure the atmospheric values collected could provide an exact comparison. The data was derived from flights 5 and 6 for the Meteodrone SSE with an average 6 minute flight duration, and flights 4 and 5 for the S2 with an average flight duration of 43.5 minutes.

Data from the flights with the Meteodrone SSE on March 4th and 6th was used to generate temperature and relative humidity analysis plots using the provided Meteomatics software. The data captured can also produce a number of derived meteorological quantities, however the temperature and humidity plots can give us an important view on the state of the ABL at time of flight.

4.4 Evaluation of Vertical Profiles

The vertical profiles in Figure 13 are obtained from the three Meteodrone flights on March 4th from 14:24 UTC to 16:10 UTC with an average flight duration of 6.25 minutes. The maximum altitude of 650 m (2133 ft) was reached on the final flight. The white peaks shown are the respective VTOL flight patterns of the Meteodrone. The shading shows the interpolated meteorological fields (Lee T. B., 2019). It is also important to note that the flight times were recorded in UTC, but the local time is set in Eastern Standard Time (EST). Thus, the flights below took place between 9:24 am to 11:10am local time (EST). During this timeframe, the ABL is in the early morning shallow convective boundary layer stage.

From the plots, we can conclude that temperature during the flights has a small range of 27 °C to 21 °C as the aircraft rises in altitude. This is indicative of the rapid growth stage of the CBL, as the cool nocturnal air is warming to a temperature similar to the residual layer thus causing the thermals to rise upward into the mixing layer. Also, the relative humidity stays

consistent around the mid 60% range until 550 m (1805 ft). After passing 550 m in altitude, the relative humidity spikes to the high 70% range. An increase in destabilization is also observed in the temperature plot, especially during the third flight around 100 m (328 ft) (Lee T. B., 2019).

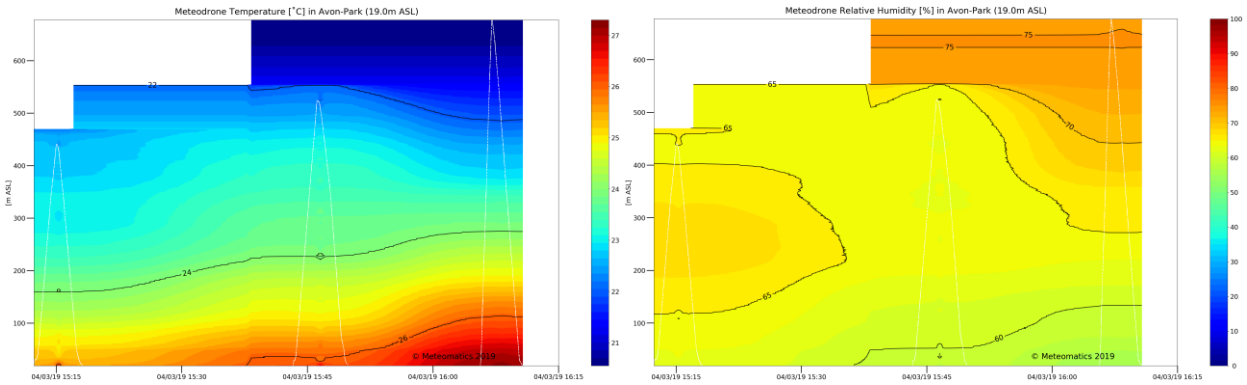

Figure 13: Evolution of Temperature (Left) and Relative Humidity (Right) Profiles on March 4 (Lee T. B., 2019)

The vertical profiles in Figure 14 are obtained from the six Meteodrone flights on March 6th from 20:23 UTC to 21:36 UTC with an average flight duration of 7.83 minutes. The maximum altitude of 950 m (3117 ft) was reached on the final flight. The flights took place between 3:23 pm to 4:10 pm local time (EST). The ABL is in the mid-afternoon convective boundary layer evolution stage. In the plots, the temperature range, 20 °C to 8 °C, is larger than the early morning flights conducted on March 4th as the aircraft rises in altitude. The instability is still increasing, and the suggested heat flux and surface temperature indicate that the expected early evening transition into the nocturnal boundary layer has not yet begun. The relative humidity shows a stagnant mid 20% range, with the occasional 18% pockets. This implies a small decrease in ABL moisture content prior to nocturnal transition. An increase in destabilization is observed in lower 30 m (98 ft) during all six flights (Lee T. B., 2019).

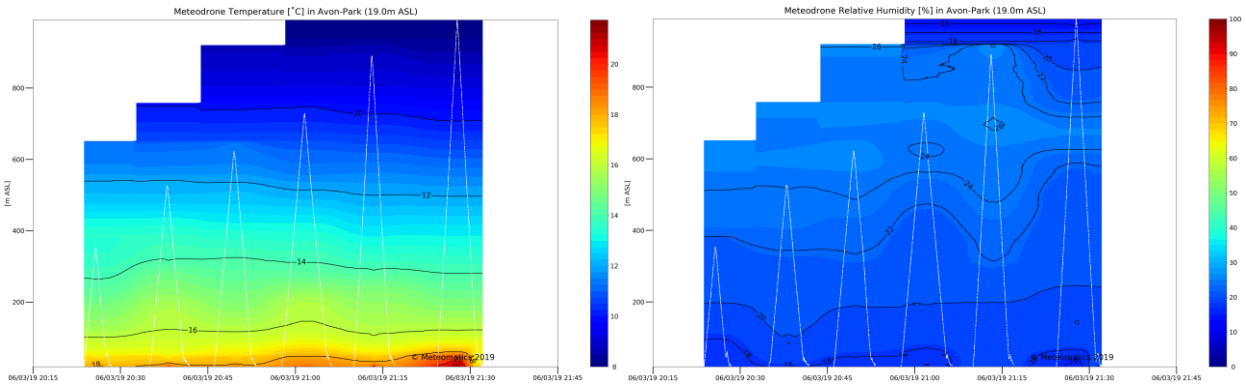

Figure 14: Evolution of Temperature (Left) and Relative Humidity (Right) Profiles on March 6 (Lee T. B., 2019)

To grow the sample size and characterize the ABL during its early morning period, additional vertical profiles were captured sporadically throughout the summer months of June, July and August 2019. These vertical profile datasets using the Meteodrone unmanned aircraft helped characterize and also served as a variable control set of the atmospheric conditions of the ABL at early morning in an open terrain setting. The vertical profiles in Figure 15 are obtained from six Meteodrone flights on June 26th from 10:23 UTC to 12:27 UTC at Oliver Springs Airport, TN with an average flight duration of 4.75 minutes. The maximum altitude of 625 m (2050 ft) was reached on all six flights.

From these plots, we can conclude that temperature during the flights has small range of 22 °C to 17 °C, with the hottest temperatures present at higher altitudes while the surface layer is cooler. This is also again indicative of the rapid growth stage of the CBL occurring during the early morning transition. Unlike the Avon Park flights, the relative humidity is extremely high around the 90% range until 375 m (1230 ft). After passing 450 m, the relative humidity falls to the mid 60% range.

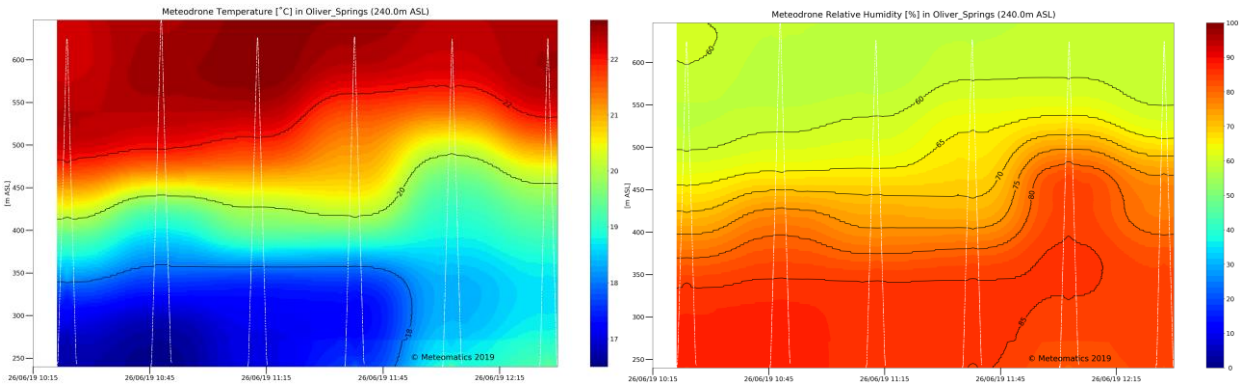

Figure 15: Evolution of Temperature (Left) and Relative Humidity (Right) Profiles on June 26

4.5 Pitfalls of UAV Data Collection in Boundary Layer

From the vertical profiles shown above, we can gather significant pertinent information about the ABL, but the constant rate of climb has under sampled the surface layer while oversampled the mixing layer during the flight durations. Additionally, by the time the unmanned aircraft returns to the ground, the boundary layer has evolved into a completely different structure, as shown by the dynamic nature occurring over multiple flights in the same observation period. The information divulged from sampling the surface layer indicates the state of the ABL at time of flight. The surface layer has wind velocity, temperature, and humidity parameters all changing swiftly with height throughout its height during these transition times. These atmospheric values will eventually reach a more constant value with height as they reach the capping inversion, as shown by the vertical profile plots in Figure 13 and 14.

Due to the consistent evolution of layers within the transitional periods, it is imperative that UAV flight plans are tailored to each layer's height to achieve a sufficient amount of sampling among the layers. Step flight profiles need to be created using the mixing length theory to optimize data sampling within the ABL at the time of each flight. Each flight path

optimization will denote the present layers during the sampling timeframe, estimate the individual layer's depth, and create a series of horizontal and vertical steps to allow enough time for sensors to evenly capture data among the transitioning layers during both the daytime and nighttime portions of the ABL diurnal cycle. All of the Avon Park flights utilized constant climb and descent rates. A major contribution of the thesis is the optimization of vertical climb profiles to provide adequate sampling resolution for each intralayer of the ABL, as detailed in Chapter 5.

CHAPTER 5

DISCUSSION OF FLIGHT PATH OPTIMIZATION

5.1 Resolution of UAV Profiles

Unmanned aircraft have the ability to perform repetitive flight maneuvers at smaller time ranges than traditionally piloted aircraft. UAV technology creates an opportunity to make difficult flight patterns without having human factors and errors present. Instead of constant vertical climb and descent rates, “stair step” flight profiling patterns can be utilized in order to adequately sample the ABL. Using this flight pattern, we can determine the temperature, relative humidity, wind velocity variables and eddy structure at optimized scales to extract the critical atmospheric information in less time. This optimization can essentially match the use of a tethered balloon system for high resolution in the lower ABL but providing the freedom of untethered flight with unlimited altitude capabilities.

The vertical gradients of the meteorological parameters, temperature, relative humidity and wind velocity, are known to be typically higher near the surface and decrease with rising altitudes, as previously mentioned. Thus, finer resolution of sampling data in the surface layer is essential for shear induced turbulence characterization. This turbulence acts to shift momentum, heat, and mass vertically within the air column. The strength of the turbulence itself varies and differs based on atmospheric stability and surface roughness (Geernaert, 2015). The surface roughness has a direct influence on the shape of the wind and temperature profiles, which in turn affects the magnitude of surface fluxes (Geernaert, 2015). Surface roughness can widely differ depending on the terrain being sampled. Surface obstacles, from scattered bushes to large metropolis buildings, have a direct impact on turbulence characteristics. In order to properly

illustrate the different type of terrain roughness, the Davenport classification system is used. In Table 5 below, the classification scale includes the aerodynamic roughness length (z_0), which is an important length scale for the surface layer, the landscape description and the corresponding drag coefficient (Wallace, 2006).

Table 5: Davenport Roughness Classification (Wallace, 2006)

Aerodynamic Roughness Scale (z_0)	Classification	Landscape	Corresponding Drag Coefficient (C_{DN})
0.0002 m	Sea	Calm sea, snow-covered flat plain, tide flat, smooth desert	0.0014
0.005 m	Smooth	Beaches, pack ice, morass, snow-covered fields	0.0028
0.03 m	Open	Grass prairie or farm fields, tundra, airports, heathers	0.0047
0.1 m	Roughly Open	Cultivated area with low crops and occasional obstacles (scattered bushes)	0.0075
0.25 m	Rough	High crops, crops of varied height, scattered obstacles (trees or hedgerows), vineyards	0.012
0.5 m	Very Rough	Mixed farm fields and forest clumps, orchards, scattered buildings	0.018
1.0 m	Closed	Regular coverage with large obstacles with open spaces roughly equal to obstacle heights, suburban houses, villages, mature forests	0.030
≥2.0 m	Chaotic	Centers of large towns and cities, irregular forests with scattered clearings	0.062

Eddy structure is also vital to adequately profiling the ABL, especially when using unmanned aircraft. As previously mentioned, eddies cascade through a succession of progressively smaller eddies until they dissipate. During the cascading succession, the internal energy of the largest eddies is transferred to the smaller eddies before dissipation. Large Eddy

Simulation (LES) of the mesoscale boundary layer currently resolves eddies down to the 25 m scale, and models the isotropic scales below 25 m. Thus, a minimum vertical solution with resolution of 25 m is an additional requirement needed for optimization.

5.2 Parameter Sampling Criteria

To create a step flight pattern for the UAVs, one needs to take into consideration the response times of the temperature, relative humidity, and wind velocity sensors. From this information, one can generate a series of horizontal and vertical steps to allow enough time for sensors to evenly capture atmospheric data among the transitioning layers. Table 6 below shows estimated sensor response times of the BlackSwift S2 and Meteomatics Meteodrone SSE for the desired parameters. It is vital to note that the horizontal wind vector is determined from the autopilot control inputs required to maintain a prescribed flight path. For our fixed-wing, S2, the aircraft should be flown as perpendicular to the mean wind as possible in order to adequately capture the horizontal wind vector.

Table 6: Sensor Response Times to ~99% of Parameters of UAVs

Parameter	BlackSwift S2	Meteodrone SSE
Temperature (°C)	0.5 seconds	1 second
Relative Humidity (%)	1 second	4 seconds
Horizontal Wind Vector	~2 seconds	~0.25 second

Additionally, we also have to address the sampling criteria of each desired parameter in order to characterize the evolving boundary layer during any portion of its diurnal cycle. For the temperature parameter, temperature values should vary with the sensible heat flux at the surface, advection, and the vertical mixing rate should be superimposed on the environment lapse rate. The lapse rate refers to the rate at which air temperature falls with increasing altitude (Stall,

2009). Strong vertical gradients will occur during advection of warm air over a cooler surface at night and the reverse, the advection of cool air over a warm surface around midday. For both of these cases, the strongest gradients exist in the near surface air of the surface layer. However, strong gradients in the upper ABL could occur if an advection of warm air over cooler air was trapped in a valley under light winds. This situation would depict inversion (Stall, 2009).

Humidity gradients are far more complex than temperature gradients. Also, humidity sensors usually have a slower response time. When the temperature changes, the relative humidity measurement will not be correct until the probe's temperature stabilizes. In theory, humidity should be at 100% only at vegetation height under healthy growing conditions and in fog/clouds. However, the humidity gradients are far more complex. Evapotranspiration, the process through which water is transferred to atmosphere via evaporation and by transpiration from plants, at the surface under cloud-free conditions will have the strongest humidity gradient. Strong humidity gradients in the upper ABL can occur during advection of fog over a warmer surface.

Similar to temperature and humidity, vertical wind gradients are also typically strongest near the surface. Thus, solidifying why the surface layer is such an intricate sublayer to adequately sample. Strong vertical wind gradients also occur near the height of the roughness lengths. These lengths come from our Davenport classification based on the terrain type. The roughness length is used as an altitude height function for the vertical wind profile.

Expected gradients of mean wind can be represented by the linear wind gradients within roughness lengths followed by a 1/7, 1/8 or 1/9 power distribution to the height of the ABL. This power law, often referred to as the wind profile power law, is the relationship between wind velocities at specified heights (Stall, 2009). In order to determine the mean wind values, we must

be able to subtract out the turbulent perturbations. Thus, presenting an issue for flight path optimizations. If encountering turbulent conditions, it could take several minutes at each fixed altitude to obtain mean horizontal wind speed values. However, we could avoid this by obtaining an instantaneous wind vector at each sampling altitude and smoothing the results to a power law distribution to approximate the mean horizontal wind.

Mixing length theory, derived from Prandtl's mixing length approach for fluid dynamics, can be used to calculate integral eddy lengths. Mixing length theory assumes that the flux is linearly proportional to and directed down the local slope (Wallace, 2006). The mixing length formula below can approximate the largest eddy lengths using the von Karman constant (k=0.4) and height (z) within the ABL.

$$l = k \times z \tag{18}$$

Using this formula, a height of 10 m (32.8 ft) in the ABL should have a production eddy length of 4 m (13.1 ft) and so forth for higher altitudes. In order to adequately sample the eddy structure, the maximum vertical interval should be 0.4*z to a maximum of 25 m. Large Eddy Simulation (LES) analysis of ABL's can currently resolve eddies to 25 m. With the parameter criteria outlined, we can now create flight path optimizations for roughly open, very rough, and closed terrain.

5.3 Optimization of Boundary Layer Sampling Routine

It is important to characterize transition periods within the diurnal cycle to adequately sample the rapidly changing boundary layer. For our optimization profiles, we chose to focus on examples of assumed early morning, midday, and nocturnal stages of the ABL. Real time ABL heights can vary depending on the atmospheric condition at the observation period. So, we can

parameterize the layer heights based off typical atmosphere boundary layer depth values for temperate continental conditions: early morning at 500 m (1640 ft), midday at 1500 m (4921 ft), and nocturnal at 300 m (984 ft). We must also estimate ABL conditions for each optimization profile. Using the weather research and forecasting model (WRF) boundary layer numerical models with the inputs of local roughness length and mesoscale synoptic conditions, we can predict the depth, external winds, and conditions within the ABL at the time of the planned observation.

To create the optimization profiles, we will cover a series of equations to derive datasets of total time of flight vs the ABL altitude heights. As previously mentioned, we are optimizing the flight paths based off of the response times for the temperature, relative humidity and wind velocity sensors on board the UAVs. Optimization profiles with emphasis on each sensor response time will be calculated for each ABL stage (early morning, midday and nocturnal) as well as an overall optimization profile of all three sensors for both unmanned aircraft. We start by sampling the winds (V) at every 0.1 m/s up to 10 m/s, where 10 m/s is our maximum wind condition (V_∞) at the top of the ABL, or any value from a WRF or other model. Using the wind profile power law and total ABL height (h), we can calculate the ABL altitude height (z/h).

$$\frac{z}{h} = \left(\frac{V}{V_\infty}\right)^7 \tag{19}$$

Once these height values have been determined, the time to climb for the specific UAV can be calculated. Shown in the formula below, time to climb can be found by taking the change in height between two positions (z/h_1, z/h_2), multiplying by the total ABL height (h), and dividing by rate of climb set by the UAV model used. For this example, 5 m/s will be used as the rate of climb velocity the Meteodrone SSE, and 15 m/s for the S2.

$$Time\ to\ Climb = \frac{\left(\frac{z}{h_2} - \frac{z}{h_1}\right) \times h}{V_{ROC}} \tag{20}$$

To adequately sample a sublayer of the ABL during its transition, the aircraft needs to collect atmospheric data once it reaches the desired altitude, fly steady until the parameter's sensor has completed the sampling, and then climb to the next desired altitude. Thus, the time to climb must be added to the sensor response time. These values added together create the total time of flight dataset. Example sensor response times for each aircraft are listed in Table 6 and were found using the UAV sensor datasheets. The desired parameter (temperature, relative humidity, or wind velocity) instrument response time will be added to the calculated time to climb values. If all atmospheric parameters are desired, a weighted function using the Simplex algorithm can be utilized to create a general sensor response time for the particular UAV. There are infinite number of sensor response time weighted functions; but for this thesis, we used the following depicted in Table 7. We chose to weight relative humidity and horizontal wind at 20% each due to their respective response times being outliers to the overall temperature response.

Table 7: Optimized Sensor Response Times for UAVs using Weighted Function

Aircraft	Temperature	Relative Humidity	Horizontal Wind	Optimized Sensor Response Time
Meteodrone SSE	60%	20%	20%	1.45 seconds
BlackSwift S2	50%	50%	N/A	0.75 seconds

Due to the small time steps, this flight maneuver needs to be extremely precise in order to fully optimize the flight plan. In order to succeed, an unmanned aircraft must be used for this step flight pattern, as it is impossible for a human pilot to mimic these maneuvers. In the next section, we will plot all the flight optimization profiles for each aircraft at the ABL stages.

5.4 Meteodrone SSE Boundary Layer Optimization Profiles

Figures 15, 16, and 17 are the optimized flight profiles for the Meteodrone SSE in the assumed early morning, midday, and nocturnal stages of the boundary layer. The desired parameter was temperature, therefore the instrument response time used to calculate the total time of flight was 1 second (see Table 6). All three plots show a step pattern that starts out in linear fashion and then develops into an exponential relationship as the time to climb increases with altitude. This change occurs around the 50 s mark for all ABL stages. Also, the total time of flight differs on each plot (200 s, 400 s, 160 s) due to the varying ABL heights based on the stage present at the observation time period.

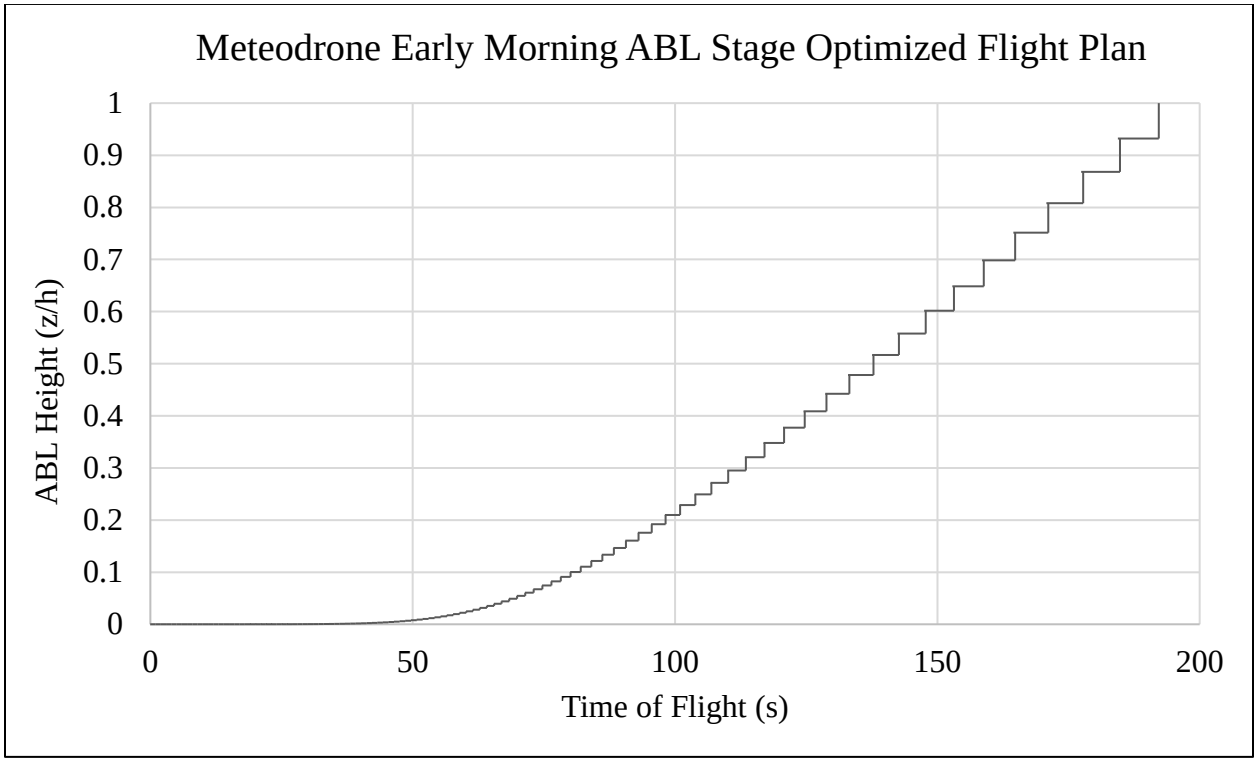

Figure 16: Meteodrone Early Morning Flight Profile (Temp Response Time)

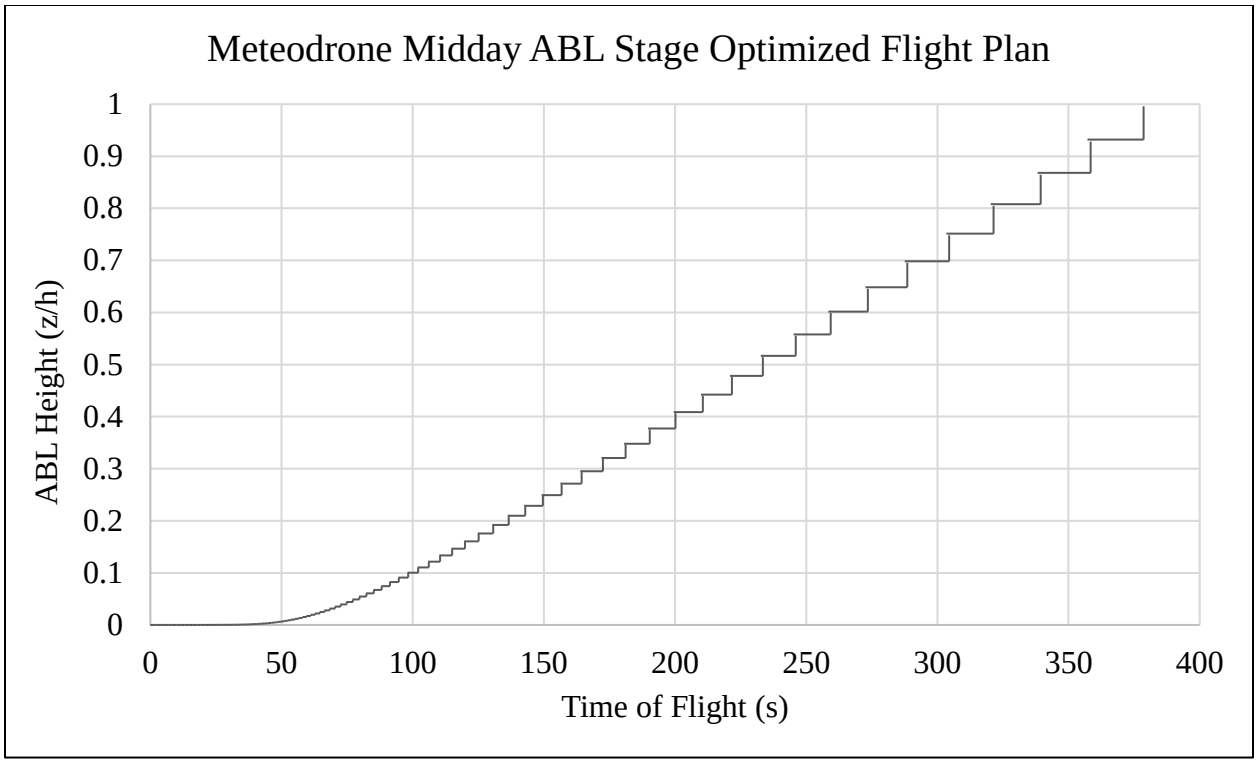

Figure 17: Meteodrone Midday Flight Profile (Temp Response Time)

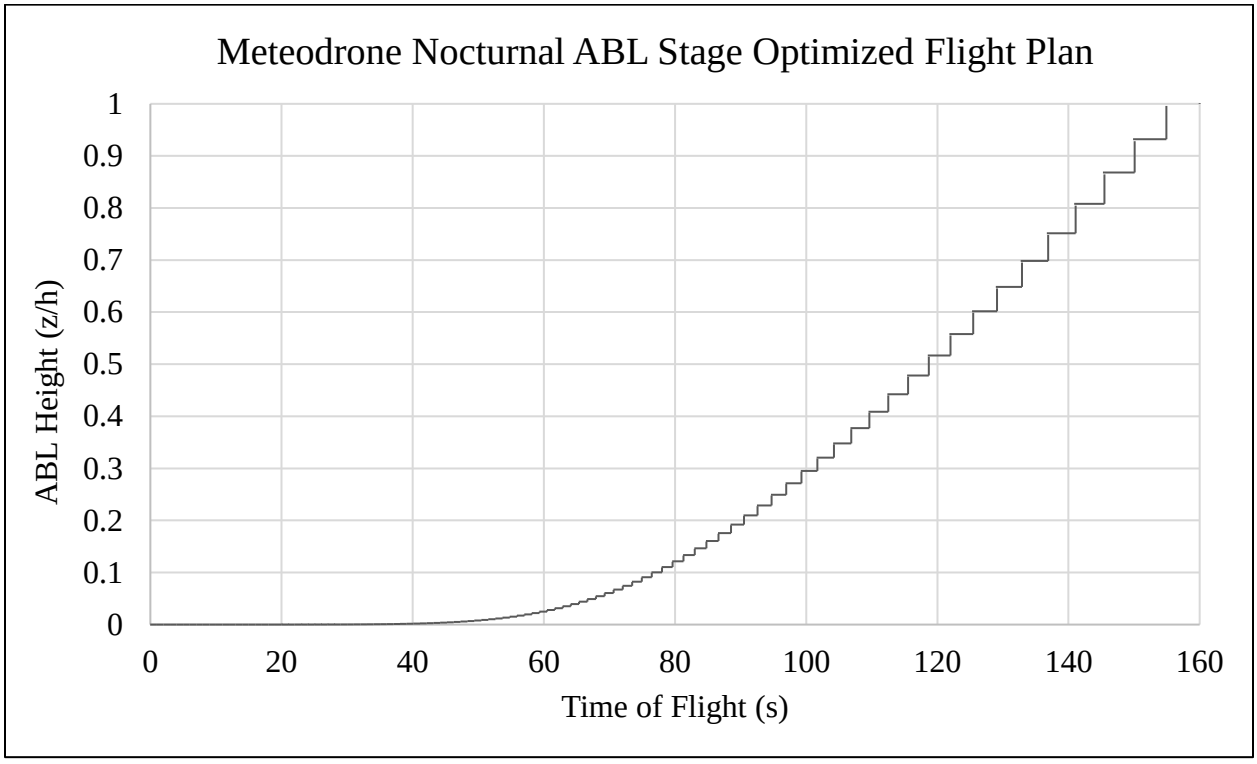

Figure 18: Meteodrone Nocturnal Flight Profile (Temp Response Time)

Figures 18, 19, and 20 are also the optimized flight profiles for the Meteodrone SSE in the early morning, midday, and nocturnal stages of the boundary layer. However, the desired parameter for these profiles is humidity, therefore the instrument sensor response time used to calculate the total time of flight was 4 seconds (see Table 6). All three plots also show a step pattern that starts out mainly as an exponential relationship and then gradually becomes linear as the time to climb increases with altitude. This happens around the 200 s mark for all ABL stages. Additionally, the total flight time needed to optimize using the humidity sensor response time is significantly longer than temperature producing total times of 500 s, 700 s, and 460 s.

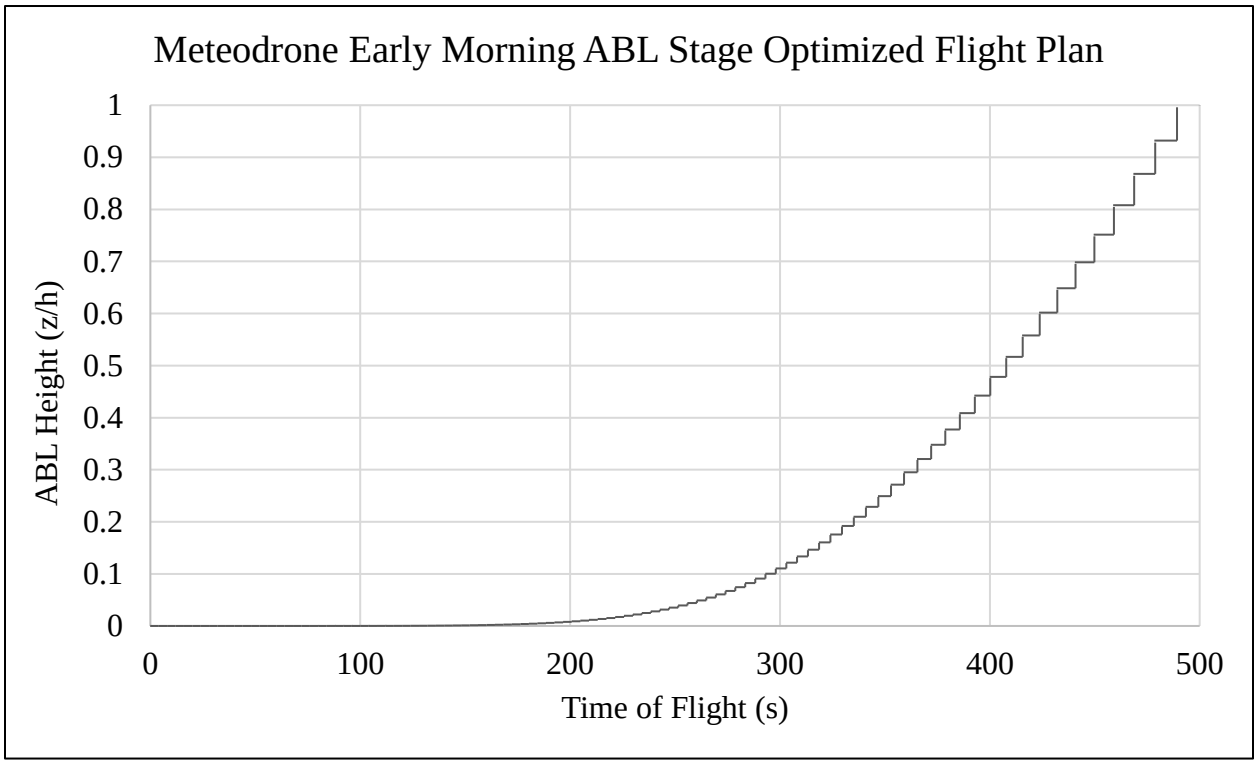

Figure 19: Meteodrone Early Morning Flight Profile (Humidity Response Time)

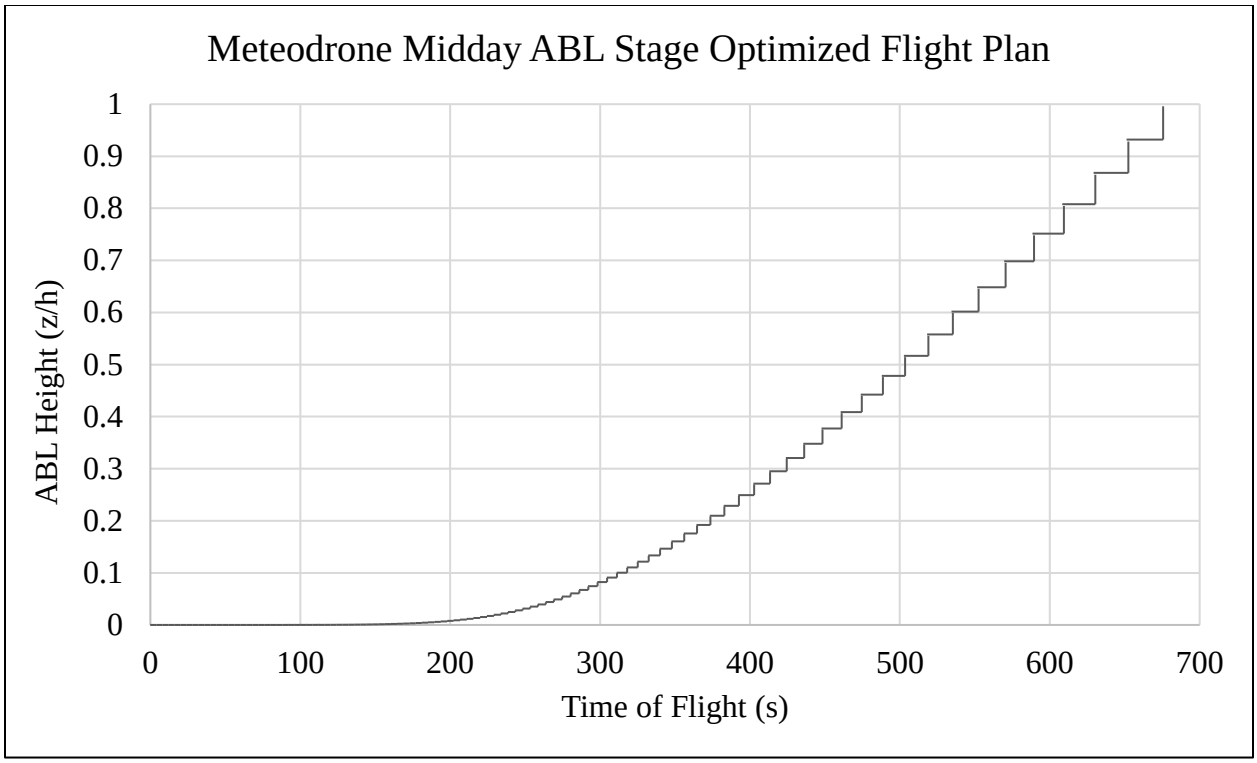

Figure 20: Meteodrone Midday Flight Profile (Humidity Response Time)

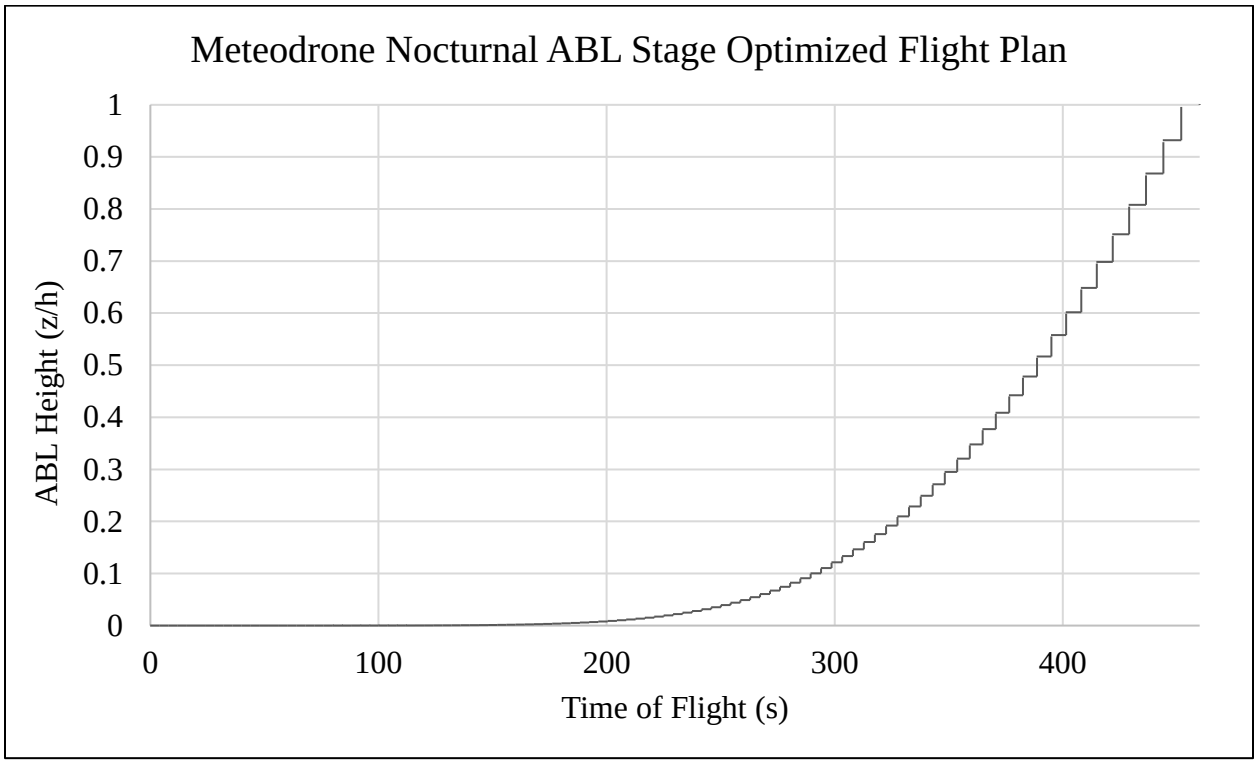

Figure 21: Meteodrone Nocturnal Flight Profile (Humidity Response Time)

Figures 21, 22, and 23 are again the optimized flight profiles for the Meteodrone SSE in the early morning, midday, and nocturnal stages of the boundary layer. However, the desired parameter for these profiles is the horizontal wind vector, therefore the instrument sensor response time used to calculate the total time of flight was 0.25 seconds (see Table 6). The total flight time needed to optimize using the humidity sensor response time is significantly shorter than both humidity and temperature producing total times of 125 s, 325 s, and 85 s. All three plots also show a step pattern that appears to be more of a linear relationship overall with a small exponential tendency at the beginning.

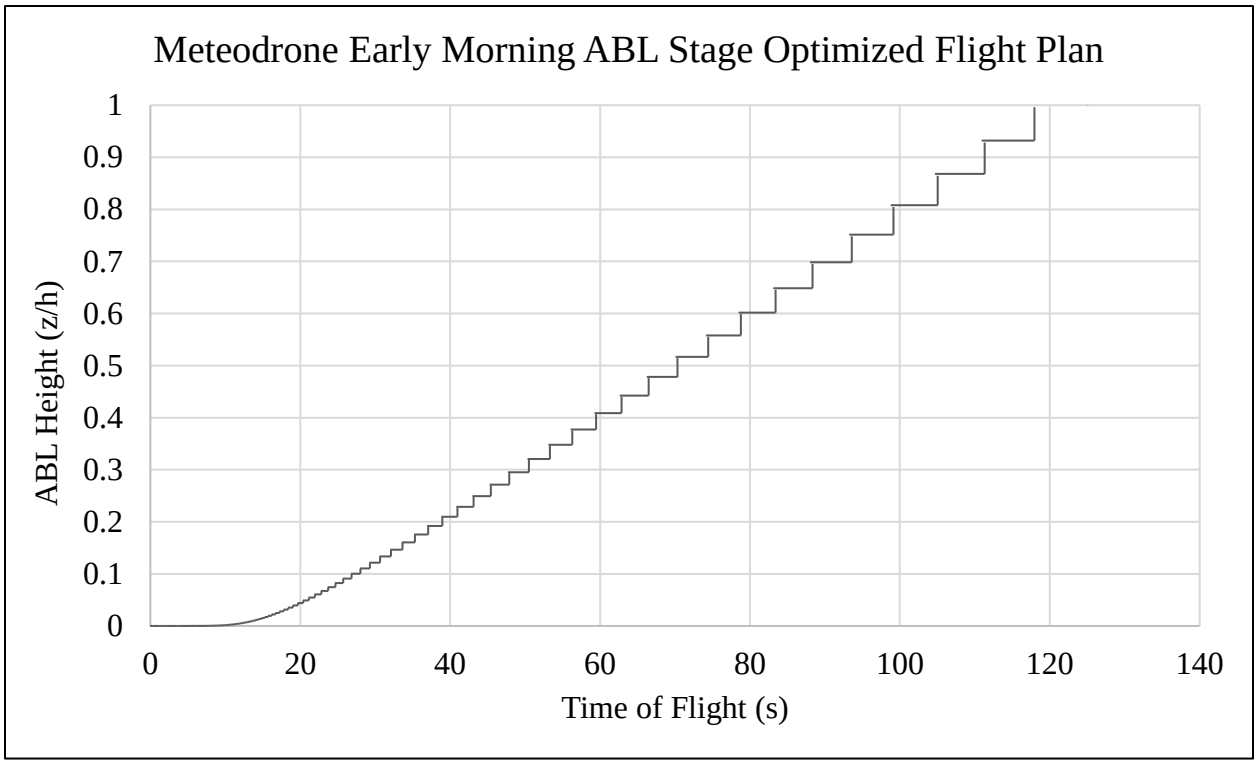

Figure 22: Meteodrone Early Morning Flight Profile (Horizontal Wind Vector Response Time)

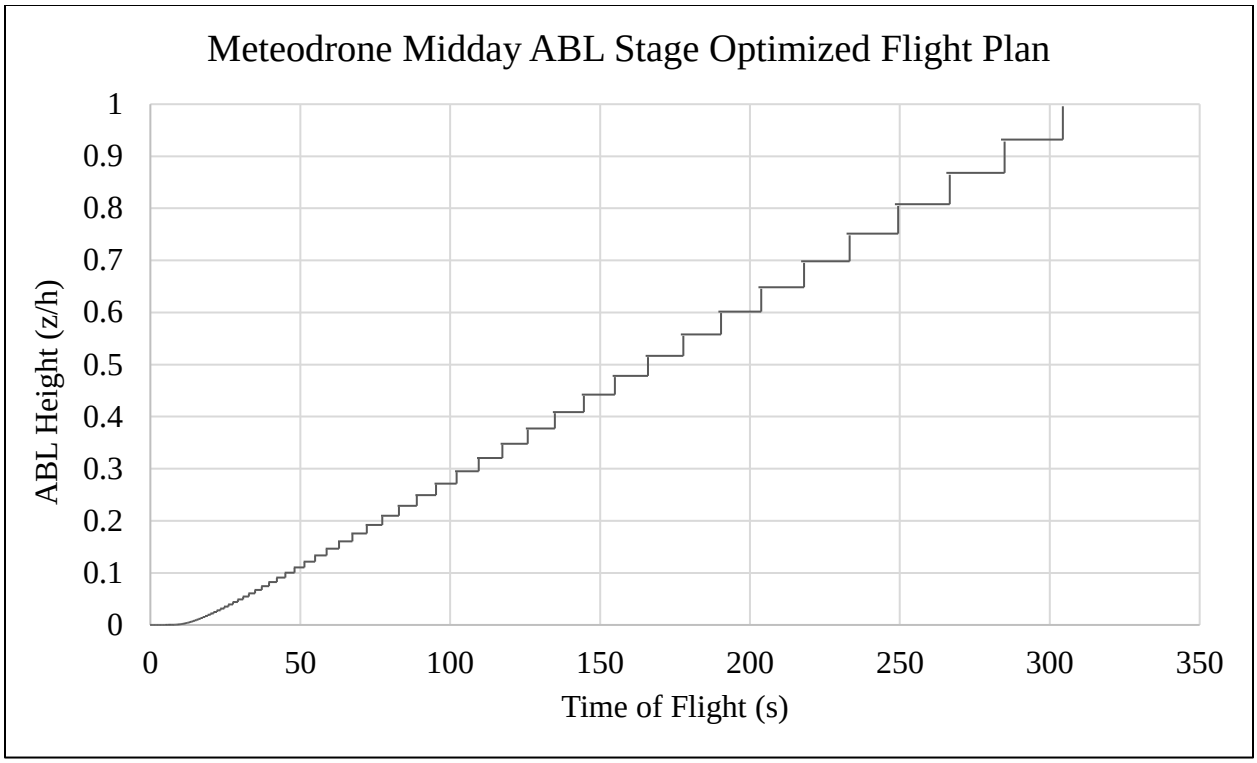

Figure 23:Meteodrone Midday Flight Profile (Horizontal Wind Vector Response Time)

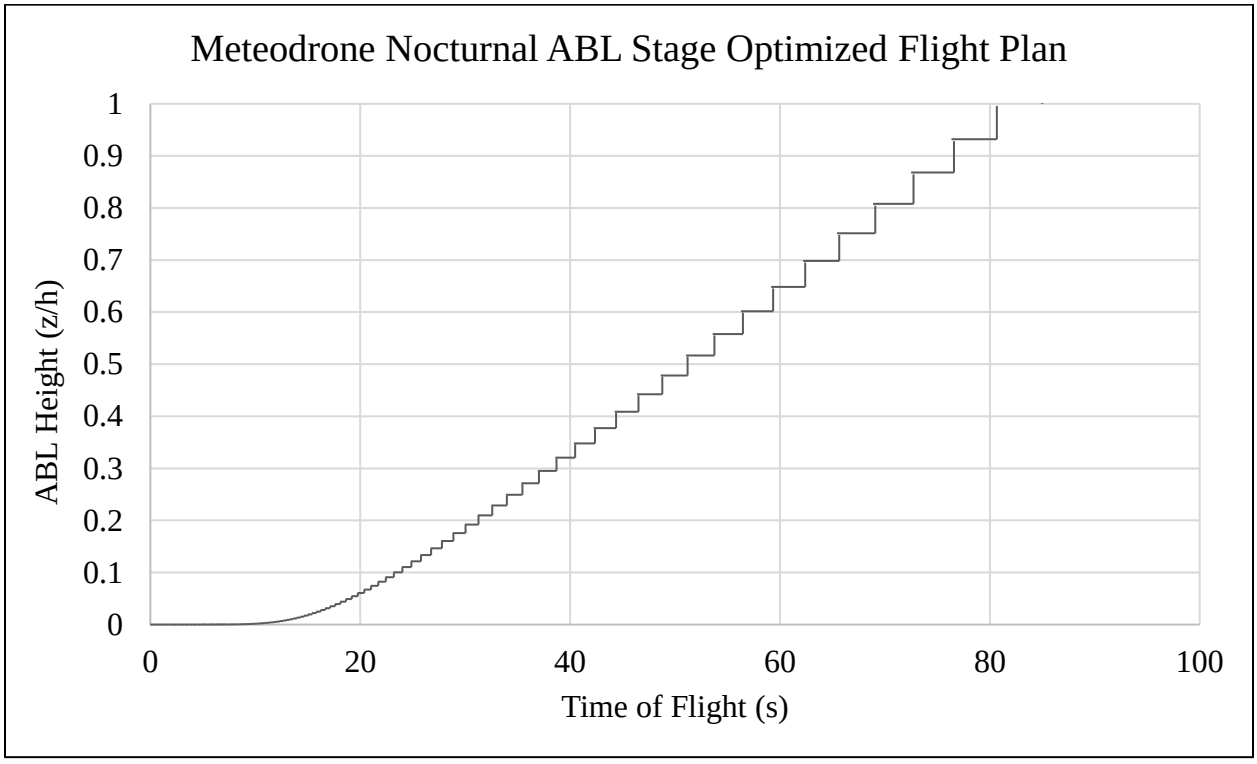

Figure 24:Meteodrone Nocturnal Flight Profile (Horizontal Wind Vector Response Time)

Using the optimized sensor response time derived by our weighted function in Table 7, the optimized flight profiles in Figures 24, 25, and 26 are for the Meteodrone SSE in the all three ABL stages. The weighted function gives us the optimized instrument response time that is used to calculate the total time of flight, 1.45 s (see Table 7). If all three atmospheric values were needed to be sampled, the following plots would be the highest resolution optimized flight patterns one could use. Similar to the temperature response time plots, all three plots also show a step pattern being as linear at small altitudes then develop into exponential relationships around 70 s. The total flight times from each plot (245 s, 445 s, 205 s) are the optimized total times of each unmanned aircraft flight, if all three atmospheric parameters were desired for sampling.

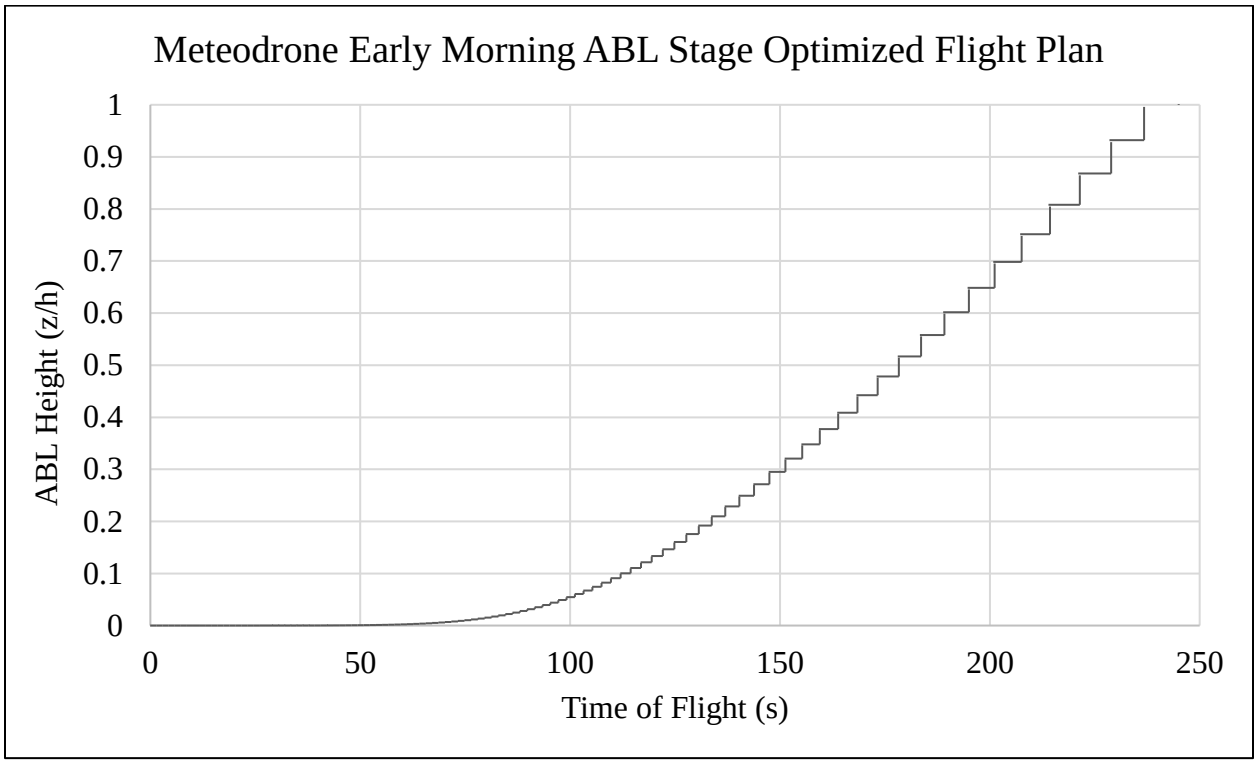

Figure 25: Meteodrone Early Morning Flight Profile (Optimized Response Time)

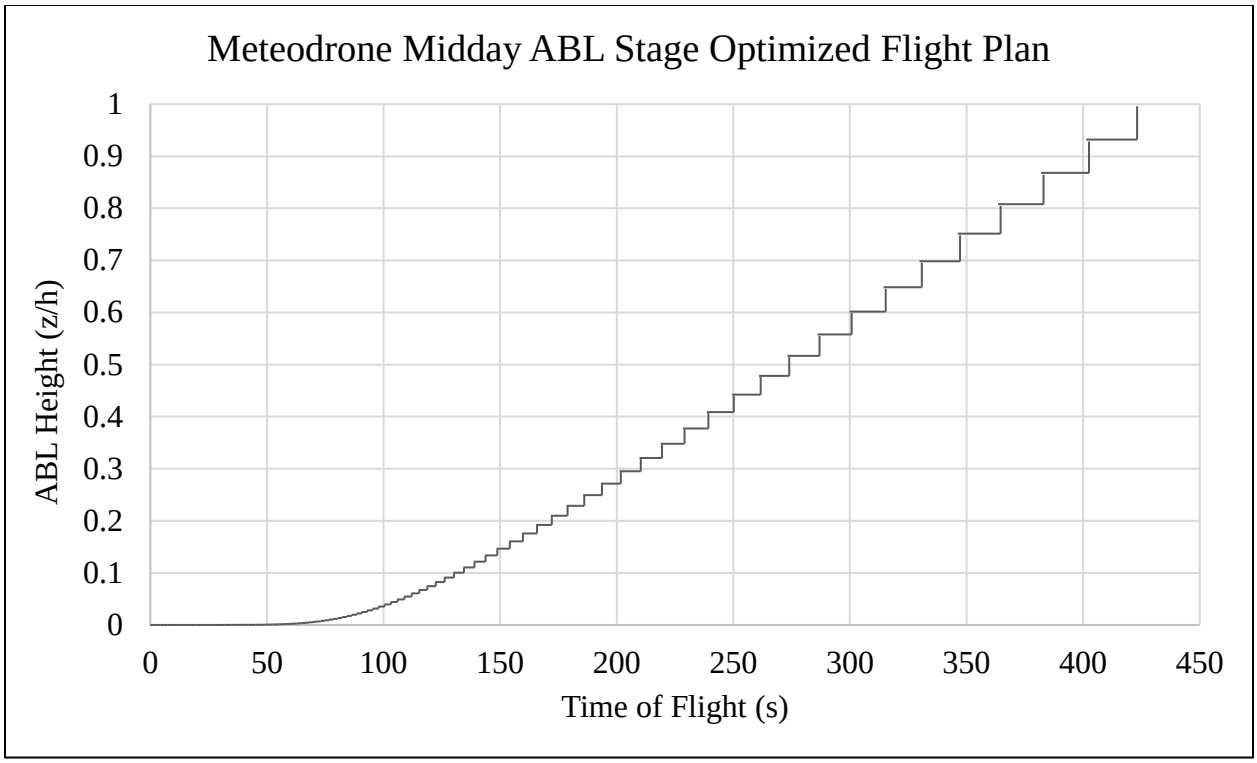

Figure 26: Meteodrone Midday Flight Profile (Optimized Response Time)

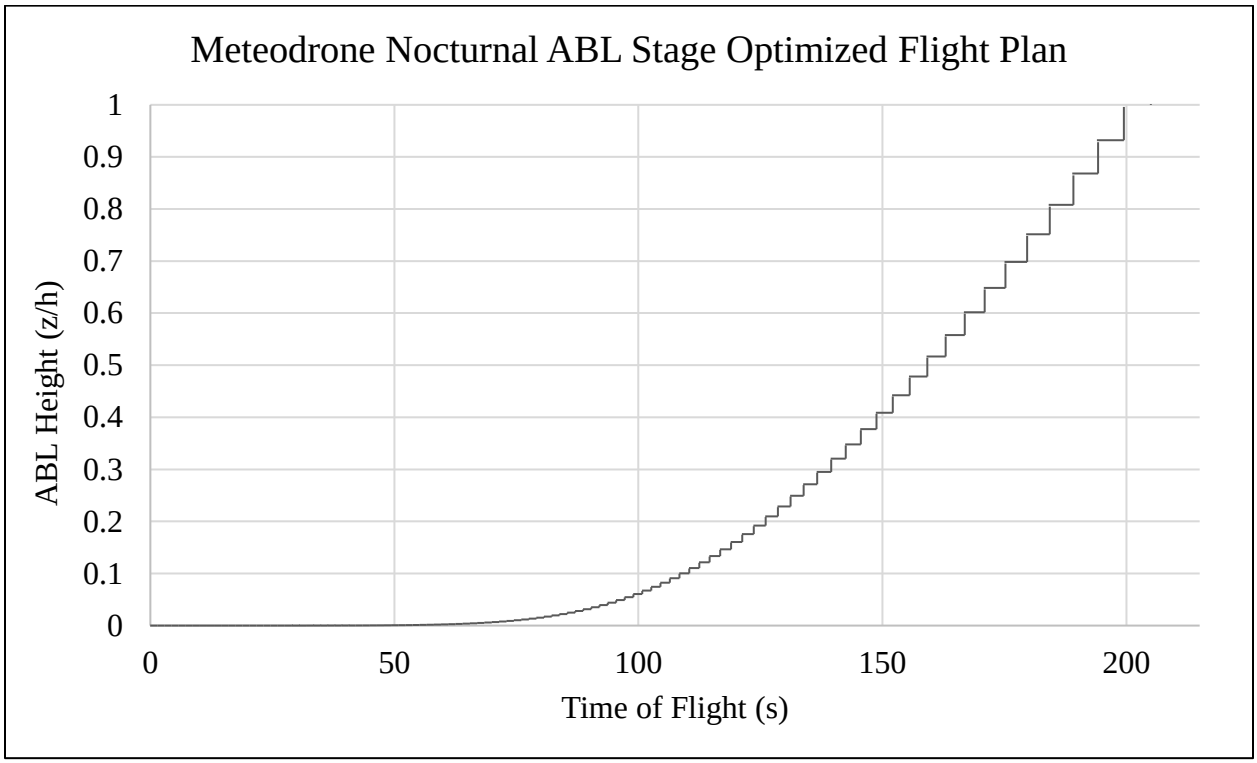

Figure 27: Meteodrone Nocturnal Flight Profile (Optimized Response Time)

5.5 BlackSwift S2 Boundary Layer Optimization Profiles

This section includes the repeated plots but for the optimized flight profiles for the BlackSwift S2 aircraft. Figures 27, 28, and 29 below are the optimized step patterns using the temperature sensor response time of 0.5 seconds (see Table 6). The plots also cover all three stages of the boundary layer: early morning, midday, and nocturnal. All three plots show a step pattern that appears to be more of a linear relationship overall with a small exponential tendency at the beginning. This change occurs around the 24 s mark for all ABL stages. It is also essential to note that the S2's rate of climb (15 m/s) is significantly faster than that of the Meteodrone (5 m/s), so we will inevitably see shorter total time of flight from the S2 overall. The total time of flight for the plots below are 83.3 s, 150 s, 70 s.

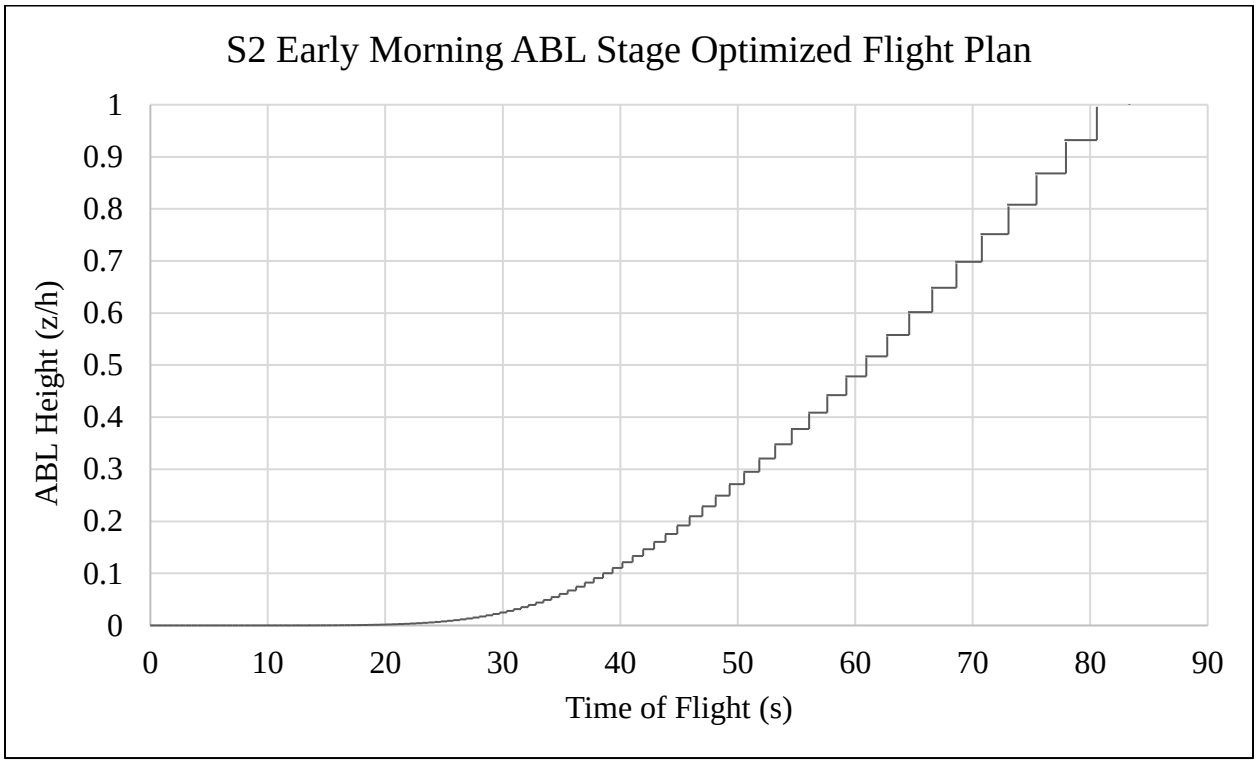

Figure 28: S2 Early Morning Flight Profile (Temperature Response Time)

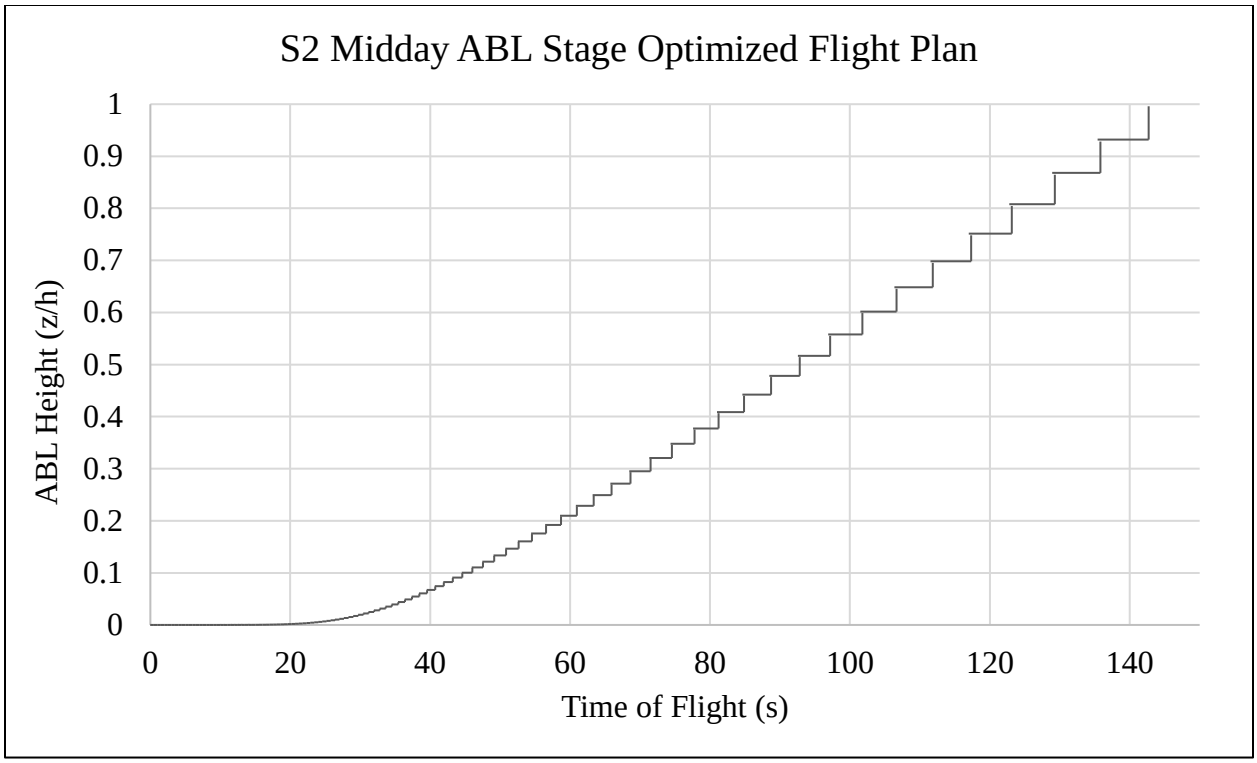

Figure 29: S2 Midday Flight Profile (Temperature Response Time)

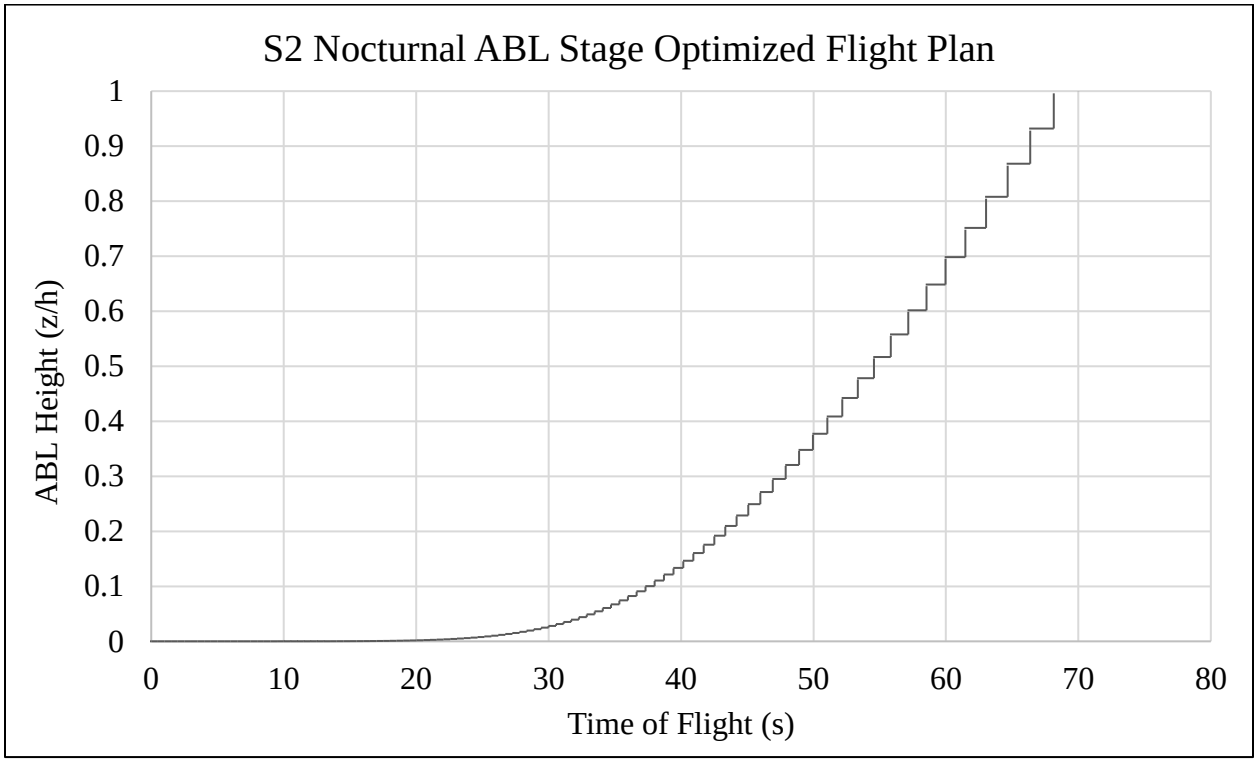

Figure 30: S2 Nocturnal Flight Profile (Temperature Response Time)

Figures 30, 31, and 32 are also the optimized flight profiles for the S2 in the assumed early morning, midday, and nocturnal stages of the boundary layer. However, the desired parameter for these profiles is humidity, therefore the instrument sensor response time used to calculate the total time of flight was 1 second (see Table 6). This is significantly shorter than the humidity sensor response time for the Meteodrone. All three plots also show a step pattern that starts out mainly as a linear relationship that becomes exponential as the time to climb increases with altitude. This happens around the 45 s mark for all ABL stages. Additionally, the total flight time needed to optimize using the humidity sensor response time is slightly longer than temperature producing total times of 133.3 s, 200 s, and 120 s.

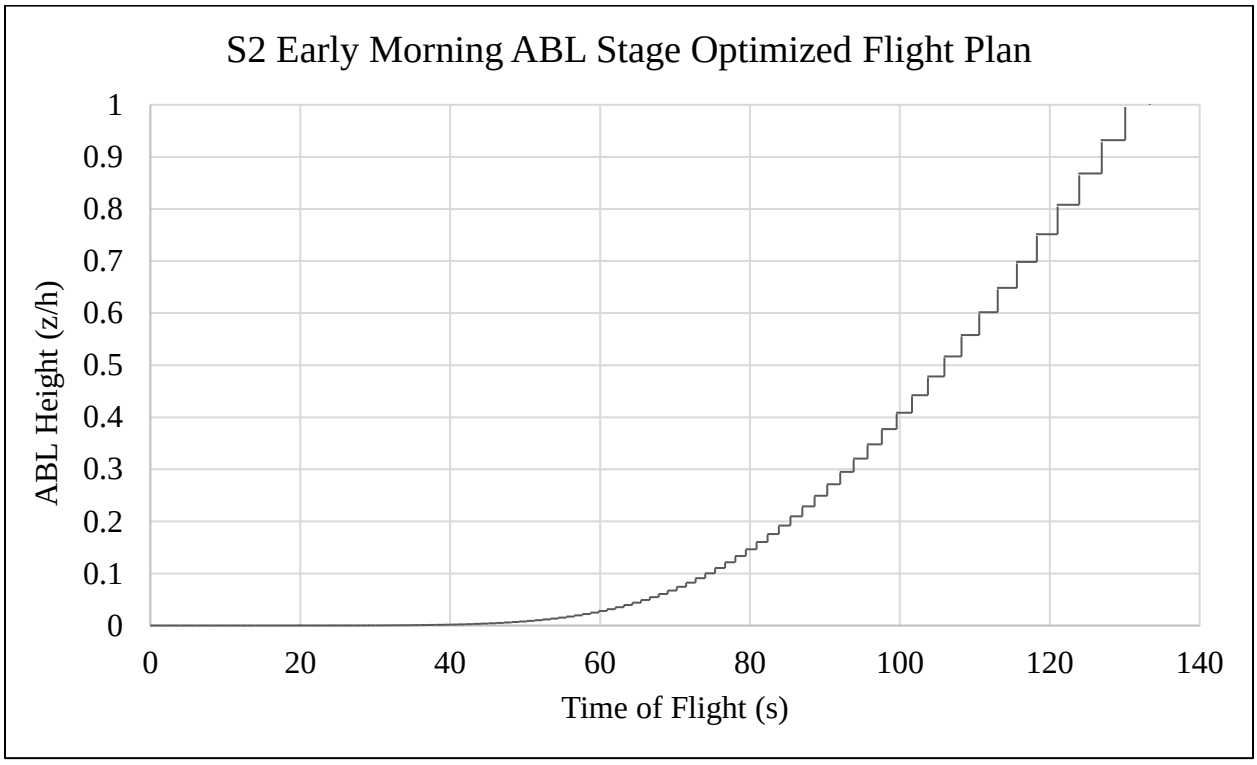

Figure 31: S2 Early Morning Flight Profile (Humidity Response Time)

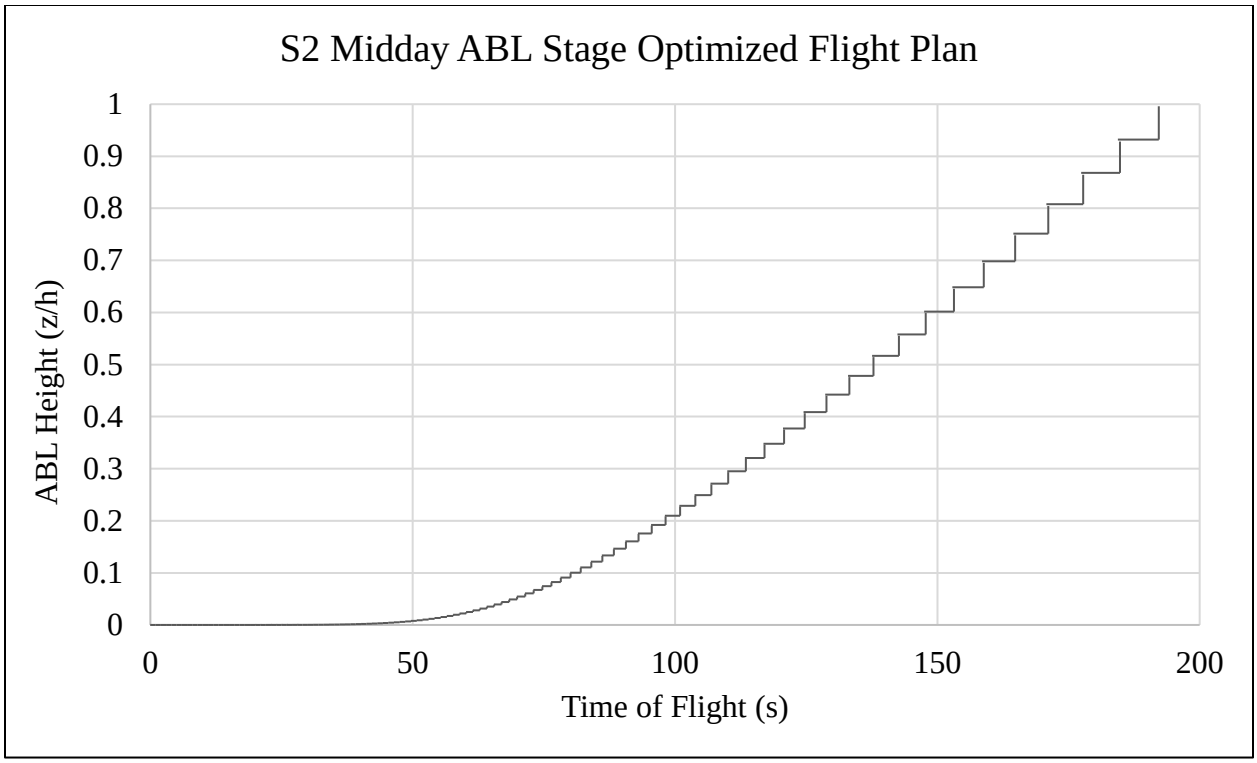

Figure 32: S2 Midday Flight Profile (Humidity Response Time)

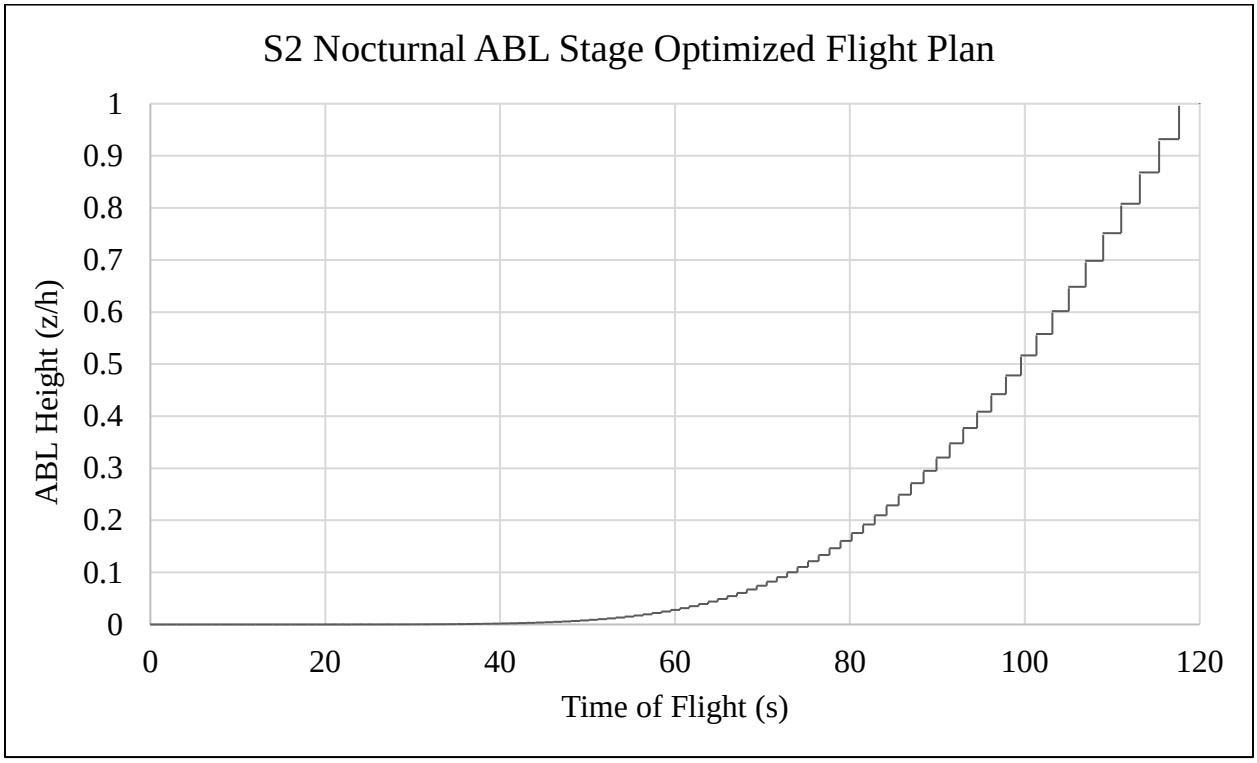

Figure 33: S2 Nocturnal Flight Profile (Humidity Response Time)

Similar to the Meteodrone, the optimized flight profiles in Figures 33, 34, and 35 are created using the optimized sensor response time derived by our weighted function in Table 7. However, this function is simpler than the Meteodrone SSE's, giving both humidity and temperature a 50% weight value. The plots are generated for all three ABL stages as well. The weighted function gives us the optimized instrument response time that is used to calculate the total time of flight, 0.75 s (see Table 7). Again, if both atmospheric parameters are required for sampling, the following plots would be the highest resolution optimized flight patterns. These plots also display a linear relationship that becomes clearly exponential around 35 s. The total flight times from each plot (108.3 s, 175 s, 95 s) are the optimized total times of each S2 unmanned flight.

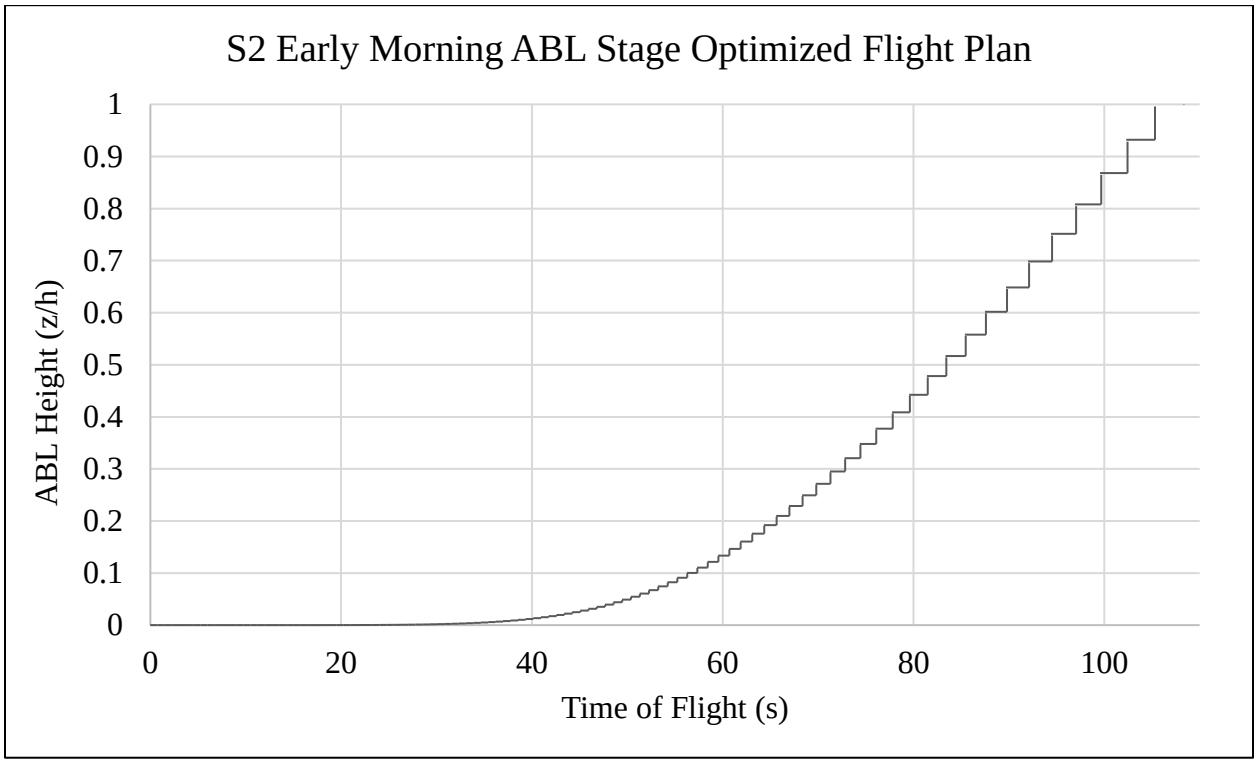

Figure 34: S2 Early Morning Flight Profile (Optimized Response Time)

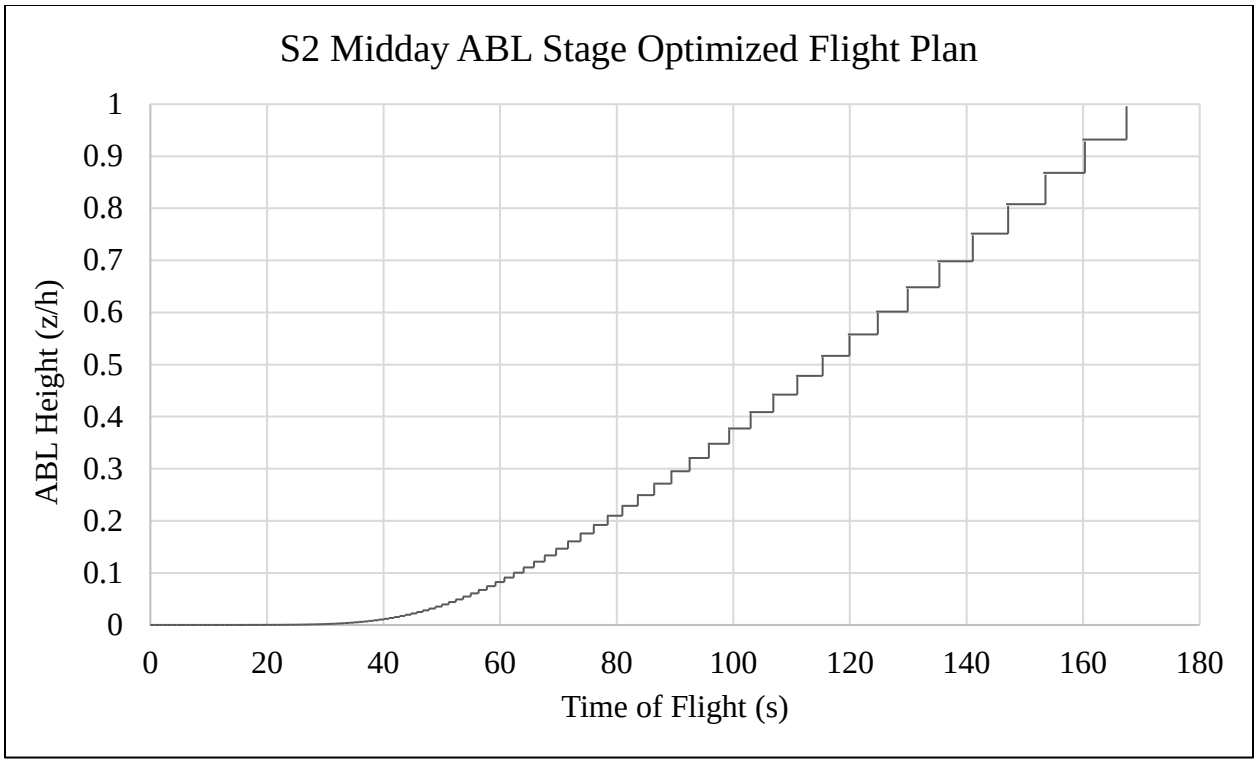

Figure 35: S2 Midday Flight Profile (Optimized Response Time)

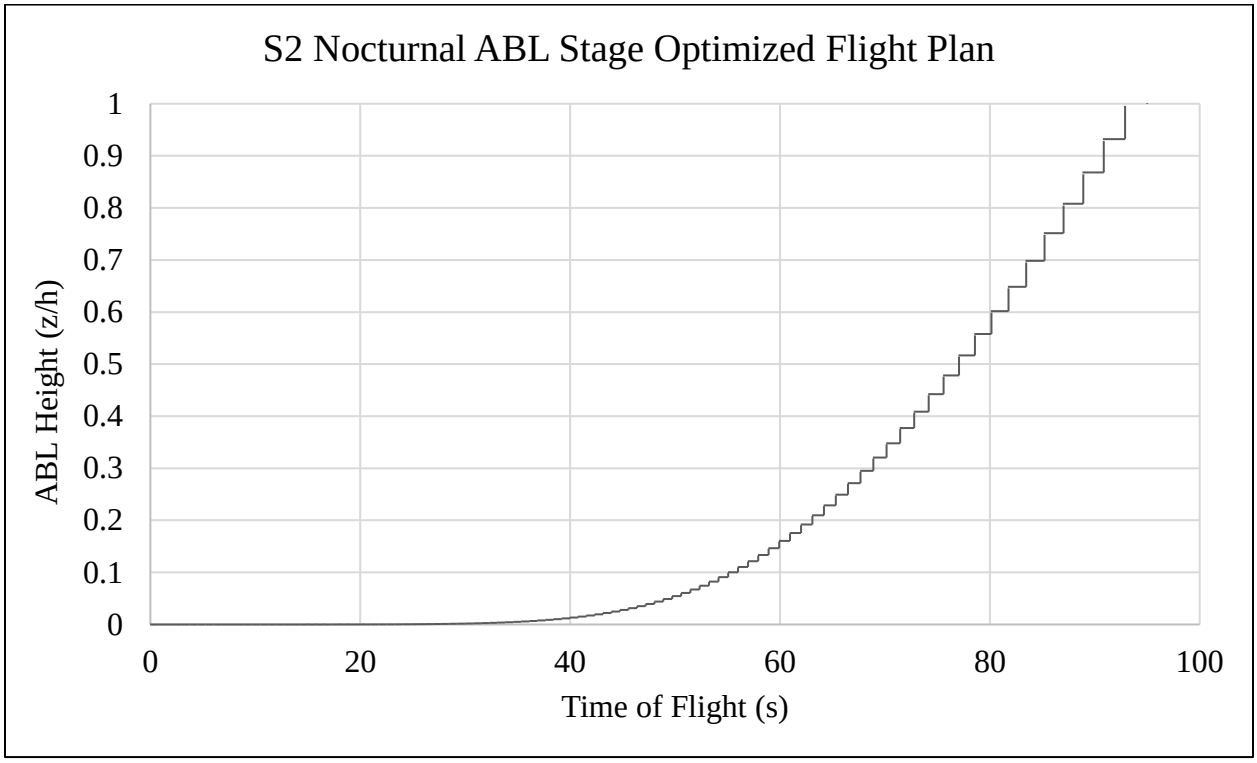

Figure 36: S2 Nocturnal Flight Profile (Optimized Response Time

CHAPTER 6

CONCLUSIONS AND FUTURE APPLICATIONS

6.1 Conclusion of Flight Profiles

Due to the consistent evolution of layers within the transitional periods, it is imperative that UAV step flight plans shown in Figures 15 through 35 are utilized in to achieve a sufficient amount of sampling among the layers. Unmanned aircraft have the ability to perform repetitive flight maneuvers at smaller time ranges, thus UAVs can be programmed to perform these step flight patterns unlike traditionally piloted aircraft. By creating weighted functions to ensure an optimized instrument response time, the profiles can be calculated with faster flight times, higher resolution of data, and adequately sample the desired parameters in the dynamic ABL. Overall, this optimization can essentially match the use of a tethered balloon system for high resolution in the lower ABL but providing the freedom of untethered flight with unlimited altitude capabilities.

Here, assumed or parameterized, sensor responses and boundary layer depths are utilized. For any particular UAV, sensors and ABL estimated conditions, these programming inputs will change, and the resultant optimized flight paths will change.

6.2 Future Usage Possibilities of UAVs

UAV technology creates an opportunity to make difficult flight patterns without having the human factors present. However, there are current industry regulations that could present issues for UAV involvement with atmospheric research. Making measurements using UAVs requires obtaining the necessary permissions from the Federal Aviation Administration (FAA). Current regulations allow NOAA to operate UAVs with visual line-of-sight up to 365 m (1200ft)

above ground level (AGL) in G class airspace (Lee T. B., 2019). The ABL depth can reach up to 3 km, or more, within its diurnal cycle, so major regulatory advancements must be made for successful integration of unmanned aircraft usage in atmospheric research to sample the entire ABL. Over the last decade, the unmanned aircraft market, commercial and research based, shows great promise and can be a thriving emerging industry for modern atmospheric sciences, agriculture, engineering, and many more disciplines.

6.3 Summary

UAV technology allows researchers to obtain higher resolution data, reduce the amount of debris contributed by radiosondes, and have a reusable system in place to satisfy the daily need for atmospheric boundary layer information that directly contributes to weather forecasting. We have flight tested fixed-wing and the rotary-wing UAVs, as reusable substitutes for the single-use balloon-borne radiosondes. The aircraft used were the rotary wing, Meteomatics Meteodrone SSE and the fixed-wing, BlackSwift S2. The aircraft gathered vertical profile measurements of temperature and relative humidity. Using a constant vertical climb and descent rates in the Avon Park experiment, both aircraft under sampled the lower regions of the ABL, while oversampling the top regions. In order to ensure adequate sampling data is captured throughout the boundary layer diurnal cycle, example flight optimization profiles were created for the assumed early morning, midday and nocturnal stages of the ABL. Optimization included an estimate of the individual layer's depth, and created a series of horizontal and vertical steps using desired parameter sensor response times to evenly capture data among the transitioning layers. Flight profile optimization can essentially match the use of a tethered balloon system for high resolution in the lower ABL but providing the freedom of untethered flight with unlimited altitude capabilities.

6.4 Recommendations for Future Work

Future applications include establishing a flight program uses the inputs of aircraft performance, roughness classification, time of day, and desired atmospheric parameter to output stair step flight patterns that can be directly programmed into the UAV's flight computer. Each computed flight path optimization can be customized to one's specific unmanned aircraft and experiment objective.

REFERENCES

Ahmed, B., & Pota, H. R. (2011). Flight Control of a Rotary Wing UAV including Flapping Dynamics. *IFAC Proceedings Volumes*, 44(1), 10373–10378. doi: 10.3182/20110828-6-it-1002.01021

Asselin, M. (1997). *An Introduction to Aircraft Performance*. Reston, VA: American Institute of Aeronautics and Astronautics.

Axisa, D., & Defelice, T. P. (2016). Modern and prospective technologies for weather modification activities: A look at integrating unmanned aircraft systems. *Atmospheric Research*, 178-179, 114–124. doi:10.1016/j.atmosres.2016.03.005

Bonin, T., Chilson, P., Zielke, B., & Fedorovich, E. (2012). Observations of the Early Evening Boundary-Layer Transition Using a Small Unmanned Aerial System. *Boundary-Layer Meteorology*, *146*(1), 119–132. doi: 10.1007/s10546-012-9760-3

Boon, M. A., Drijfhout, A. P., & Tesfamichael, S. (2017). Comparison of A Fixed-Wing and Multi-Rotor UAV for Environmental Mapping Applications: A Case Study. *ISPRS - International Archives of the* (Boon, 2017) *Photogrammetry, Remote Sensing and Spatial Information Sciences*, *XLII-2/W6*, 47–54. doi: 10.5194/isprs-archives-xlii-2-w6-47-2017

Bruin, A. D., & Jones, T. (2016). Accurate Autonomous Landing of a Fixed-Wing Unmanned Aircraft under Crosswind Conditions. *IFAC-PapersOnLine*, 49(17), 170–175. doi: 10.1016/j.ifacol.2016.09.030

Chen, W., Lovejoy, S., & Muller, J.-P. (2016). Mars Atmosphere: The sister planet, our statistical twin. *Journal of Geophysical Research: Atmospheres*, 121(20). doi: 10.1002/2016jd025211

Cornman, L. B., Morse, C. S., & Cunning, G. (1995). Real-Time Estimation of Atmospheric Turbulence Severity from In-Situ Aircraft Measurements. *Journal of Aircraft*, 32(1), 171–177. doi: 10.2514/3.46697

Elston, J., Argrow, B., Stachura, M., Weibel, D., Lawrence, D., & Pope, D. (2015). Overview of Small Fixed-Wing Unmanned Aircraft for Meteorological Sampling. *Bull. Amer. Meteor. Soc*. doi: 10.1175/JTECH-D-13-00236.1

Flores, F., R. Rondanelli, M. Díaz, R. Querel, K. Mundnich, L.A. Herrera, D. Pola, and T. Carricajo, 2013: The Life Cycle of a Radiosonde. *Bull. Amer. Meteor. Soc.*, *94*, 187–198. doi: 10.1175/BAMS-D-11-00163.1

Geernaert, G. L. (2015). BOUNDARY LAYER (ATMOSPHERIC) AND AIR POLLUTION | Surface Layer. In *Encyclopedia of Atmospheric Sciences* (2nd ed., pp. 305–309). San Diego, CA: Elsevier. doi: 10.1016/B978-0-12-382225-3.00092-X

Hardin, L., Tillman, G., Sharma, O., Berton, J., & Arend, D. (2012). Aircraft System Study of Boundary Layer Ingesting Propulsion. *48th AIAA/ASME/SAE/ASEE Joint Propulsion Conference & Exhibit*. doi: 10.2514/6.2012-3993

Hassanalian, M., Rice, D., Johnstone, S., & Abdelkefi, A. (2018). Performance Analysis of Fixed Wing Space Drones in Different Solar System Bodies. *Acta Astronautica*, 152, 27–48. doi: 10.1016/j.actaastro.2018.07.018 (Chen, 2016)

Hemingway, B., Frazier, A., Elbing, B., & Jacob, J. (2017). Vertical Sampling Scales for Atmospheric Boundary Layer Measurements from Small Unmanned Aircraft Systems (sUAS). *Atmosphere*, *8*(12), 176. doi: 10.3390/atmos8090176

Koch, S. E., Fengler, M., Chilson, P. B., Elmore, K. L., Argrow, B., Andra, D. L., & Lindley, T. (2018). On the Use of Unmanned Aircraft for Sampling Mesoscale Phenomena in the Preconvective Boundary Layer. *Journal of Atmospheric and Oceanic Technology*, *35*(11), 2265–2288. doi: 10.1175/jtech-d-18-0101.1

Lee, T., Buban, M., Dumas, E., & Baker, C. (2018). On the Use of Rotary-Wing Aircraft to Sample Near-Surface Thermodynamic Fields: Results from Recent Field Campaigns. *Sensors*, *19*(1), 10. doi: 10.3390/s19010010

Lee, T., Buban, M., Dumas, E., & Baker, C. (2019). Improved Sampling of the Atmospheric Boundary Layer Using Small Unmanned Aircraft Systems: Results from the Avon Park Experiment (*NOAA Technical Memorandum OAR ARL-279*). Oak Ridge, TN: Atmospheric Turbulence and Diffusion Division.

Panagiotou, P., & Yakinthos, K. (2019). Aerodynamic Efficiency and Performance Enhancement of Fixed-Wing UAVs. *Aerospace Science and Technology*, 105575. doi: 10.1016/j.ast.2019.105575

Petrosyan, A., Galperin, B., Larsen, E., Lewis, S. R., Määttänen, A., Read, P. L., … Vázquez, L. (2011). The Martian Atmospheric Boundary Layer. *Rev. Geophys*, *49*. doi: 10.1029/2010RG000351

Pommereau, J. P., Dabberdt, W. F., & Turtiainen, H. (2003). OBSERVATION PLATFORMS | Balloons, Radiosondes. *Encyclopedia of Atmospheric Sciences*, 1429–1438. doi: 10.1016/b0-12-227090-8/00254-2

Prudden, S., Fisher, A., Marino, M., Mohamed, A., Watkins, S., & Wild, G. (2018). Measuring Wind with Small Unmanned Aircraft Systems. *Journal of Wind Engineering & Industrial Aerodynamics*, (176), 197–210. doi: 10.1016/j.jweia.2018.03.029

Rotaru, C., & Todorov, M. (2018). Helicopter Flight Physics. *Flight Physics - Models, Techniques and Technologies*. doi: 10.5772/intechopen.71516

Stall, R. B. (2009). *An Introduction to Boundary Layer Meteorology.* New York: Springer

Stratum, B. J. H. V., & Stevens, B. (2015). The Influence of Misrepresenting the Nocturnal Boundary Layer on Idealized Daytime Convection in Large-eddy Simulation. *Journal of Advances in Modeling Earth Systems*, 7(2), 423–436. doi: 10.1002/2014ms000370

Wallace, J. M., & Hobbs, P. V. (2006). *Atmospheric Science: An Introductory Survey*. Amsterdam: Elsevier.

Wingo, S. M., & Knupp, K. R. (2014). Multi-platform Observations Characterizing the Afternoon-to-Evening Transition of the Planetary Boundary Layer in Northern Alabama, USA. *Boundary-Layer Meteorology*, *155*(1), 29–53. doi: 10.1007/s10546-014-9988-1

Wragg, D. W. (2008). *Historical Dictionary of Aviation: From Earliest Times to the Present Day*. Stroud, Gloucestershire: History Press.

VITA

Brittany Lane Porcelli was born in Fayetteville, North Carolina on July 9, 1993 to Frank and Sherri Jenio. She and her two younger siblings, Emma Jenio and Zack Jenio, were raised in an active duty military family frequently moving across the US to multiple army bases. After being stationed in Ft. Bragg, North Carolina, Brittany graduated from Fayetteville Terry Sanford High School in 2011. She graduated from North Carolina State University in Raleigh, NC with a Bachelor of Science in Materials Science Engineering in 2016. Post-graduation, Brittany accepted a position as a Materials Design Engineer at United Technologies Aerospace Systems in Wilson, North Carolina. In 2018, Brittany accepted a graduate research assistantship at the University of Tennessee Space Institute to pursue a Master of Science in Aerospace Engineering, Applied Mechanics concentration under Steve Brooks. After obtaining her degree, she will join the aviation industry and begin an Aerospace Engineer position in Denver, Colorado.